The effect of temperature on the equilibrium distribution of trace elements between clinopyroxene, orthopyroxene, olivine and spinel in upper mantle peridotite

Gudrun Witt-Eickschen[a], Hugh St.C. O'Neill[b],*

[a]*Institut für Mineralogie und Geochemie der Universität Köln, Zülpicher Str. 49b, D-50674 Köln, Germany*
[b]*Research School of Earth Sciences, Australian National University, Canberra, ACT 0200, Australia*

Abstract

The abundance of 30 trace elements has been determined in the minerals of 16 well-equilibrated spinel lherzolite xenoliths by laser-ablation inductively-coupled-plasma mass-spectrometry (LA-ICP-MS). Major elements were analysed by electron microprobe. The xenoliths span a range of equilibration temperatures from 1150 to 1500 K (calculated at an assumed pressure of 1.5 GPa from two-pyroxene geothermometry), allowing the trace-element partitioning relationships among the phases (olivine, orthopyroxene, clinopyroxene, spinel, and in some lower temperature xenoliths, amphibole) to be quantified as a function of temperature. Most elements show smooth partitioning trends among all phases that depend primarily on temperature but with some influences from bulk composition, particularly the amount of Na in clinopyroxene. Although most incompatible trace elements are concentrated into clinopyroxene, the effect of increasing temperature is to redistribute these elements into orthopyroxene and even olivine, such that these latter phases hold non-negligible proportions of many trace elements at the temperature at which peridotite would be in equilibrium with basaltic melts. The inter-crystalline trace-element partition coefficients reported in this study can be used to reconstruct the trace-element abundances in clinopyroxene at melting temperatures, and should also prove useful in elucidating the histories of more complex mantle peridotites with unequilibrated mineral compositions and textures.
© 2005 Elsevier B.V. All rights reserved.

Keywords: Trace-element partitioning; Upper mantle; Peridotite

1. Introduction

Peridotites derived from the upper mantle but available at the Earth's surface for geochemical and petrological investigation are generally thought to be residues of the partial melting that produces basalt.

* Corresponding author. Tel.: +61 2 6125 5159; fax: +61 2 6125 5989.
  E-mail address: hugh.oneill@anu.edu.au (H.St.C. O'Neill).

The trace-element geochemistry of these peridotites have often been studied to constrain better the melting and melt-extraction processes, but such an approach has several potential pitfalls arising from the complex subsolidus history of the peridotites subsequent to the melt-extraction event. In particular, many peridotites are partially serpentinized or otherwise altered, which has provided an incentive to examine the trace-element patterns of individual phases as an alternative to the probably contaminated whole-rock values; this approach has been made technically possible through the development of SIMS, and latterly laser-ablation ICP-MS microanalytical techniques. However, mantle peridotites have generally recrystallized subsolidus, which must result in the redistribution of trace elements among the phases. In order to carry out modelling of melting relations, it is therefore necessary to reconstruct the compositions of mineral phases at the temperature at which they would be in equilibrium with melt. This requires knowing how the trace elements redistribute during cooling.

The goal of this work is to determine the required intercrystalline trace-element partition coefficients as a function of temperature for a wide variety of trace elements (including most of those used in geochemical modelling) for the spinel-lherzolite facies, by using a set of 16 well-equilibrated spinel-lherzolite xenoliths covering a large range of equilibration temperatures as a set of natural experiments. In addition to this primary aim, a more detailed knowledge of intercrystalline equilibrium trace-element partitioning relations should be useful for checking internal consistency in sets of mineral/melt partition coefficients used in geochemical modelling; for reconstructing original melt compositions of melt inclusions; and for insights into the crystal-chemical controls on trace-element substitutions, which are needed for more reliable thermodynamic modelling of partition coefficients. We also envisage that the temperature-dependent partition coefficients established in this work will help in elucidating the petrologic histories of more complex peridotites that preserve textural and geochemical evidence of melt infiltration, metamorphic differentiation and other mantle processes.

Previous work using mineral separates (e.g., Stosch, 1982; Bedini and Bodinier, 1999) and the microanalytical techniques of the electron microprobe (McDonough et al., 1992), SIMS (Hervig et al.,

1980), PIXE (e.g., O'Reilly et al., 1991) and laser-ablation ICP-MS (e.g., Norman et al., 1998) has built up a basic understanding of trace-element distributions among peridotite minerals. We draw particular attention to the detailed LA-ICP-MS study of Eggins et al. (1998), which established the approach used in this study.

2. Analytical procedures

Major element analyses were performed on a JEOL JXA8900 electron-microprobe (Institut für Mineralogie und Geochemie der Universität Köln, Germany) under standard conditions (20 kV accelerating voltage, 20 nA beam current, focussed 1 μm beam, 20–100 s counting time depending upon the element). A set of synthetic silicates (for Si, Mg, Ca, Na, K, Mn, Fe) and oxides (for Al, Cr, Ti, Ni) was used for standardization, and data were corrected using the ZAF-algorithm.

Trace elements were measured in situ on polished thin sections by laser ablation inductively coupled plasma mass spectrometry (LA-ICP-MS) at the Research School of Earth Sciences, Australian National University. Ablation was performed in a He atmosphere by an ArF Excimer laser (193 nm) with a pulse energy of 100 mJ and a 5 Hz pulse repetition rate; the ablation time was 60 s. The ablated material was flushed in a continuous argon flow into the torch of an Agilent 7500 Series ICP-MS. Before and after ten unknowns the silicate glass reference material NIST 612 (National Institute of Standards and Technology) and the background count rates were measured for calibration purposes and instrumental drift corrections. To correct for differences in the ablation yield between standard and samples, ^{43}Ca (for clinopyroxene, orthopyroxene and amphibole) and ^{24}Mg (for olivine and spinel) were used as an internal standard, based on the electron-microprobe measurements of CaO and MgO in the minerals. Further information about analytical details including correction procedures, limits of detection, and instrumental errors are described in Eggins et al. (1998). For each mineral, 1–12 analyses with an 84 μm laser spot size were performed within the grain cores.

The quality of the analyses was continually checked throughout the analytical campaign (which

covered two months) on the basalt glass standard USGS BCR-2G. This resulted in 307 replicate analyses, which establish the long-term precision of the method. In Table 1 the average of these analyses is compared with the data published by Norman et al. (1998).

The abundances of Sr, Nd, Sm, and Pb have previously been determined for some separates of clinopyroxene and amphibole by isotope dilution and thermal ionization mass spectrometry (TIMS) using a VG Sector 54 spectrometer (Institut für Mineralogie der Universität Münster, Germany). Pure separates were obtained by hand-picking under a binocular microscope, followed by ultrasonic washing in ultrapure water, and leaching either in cold HF–HNO$_3$ (5:1) for 15 min (Sr, Nd, Sm) or in

hot 2N HCl for 2 h (Pb). The separates were spiked with mixed ^{87}Rb–^{84}Sr and ^{149}Sm–^{146}Nd spikes, or a ^{205}Pb spike, respectively, and decomposed with HF–HNO3 (5:1). A description of the cation exchange techniques, the measurement conditions and correction procedures for mass fractionation has been given in Witt-Eickschen and Kramm (1997) and Witt-Eickschen et al. (2003). The comparison with the present results for these elements is given in Fig. 1a.

The results of this LA-ICP-MS study may also be compared with previously published trace element data (Witt-Eickschen and Harte, 1994) for clinopyroxene and amphibole determined by secondary ion mass spectrometry (SIMS). The SIMS analyses were carried out in situ on the same thin sections with a

Table 1
Results of LA-ICP-MS analyses on BCR-2G (n.a.=not analysed)

| Element (isotope measured)	This work (N=307)			Norman et al. (1998)	Barth et al. (2001)	Gao et al. (2002)	Halicz and Günther (2004)
	Mean	S.D.	% S.D.				
P 31	1625	136	8.3	1615	n.a.	n.a.	n.a.
Sc 45	31.9	0.4	1.4	33	35.1	32	n.a.
Ti 47	13,714	448	3.3	13,700	15,227	13,005	13,900
V 51	436	6	1.5	414	423	425	454
Cr 53	17.2	1.1	6.3	18.8	17	17	17
Co 59	41.0	0.9	2.1	36	n.a.	38	42
Ni 60	13.0	0.4	2.8	10.8	13	12.7	14
Ga 69	25.6	0.5	1.8	22.7	22	24	25
Rb 85	54.2	1.1	2.0	49	48.6	51	52
Sr 88	336	6	1.7	342	318	321	338
Y 89	34.5	0.7	2.1	35.3	31.5	31	n.a.
Zr 90	183	3	1.9	194	165	167	195
Zr 91	183	4	2.0	n.a.	n.a.	n.a.	n.a.
Nb 93	13.1	0.2	1.5	12.8	11.7	10.9	n.a.
Ba 138	681	22	3.2	660	647	641	646
La 139	24.5	0.5	2.0	24.5	23.9	25	25
Ce 140	52.3	1.0	1.8	50.5	49.3	52	51
Nd 146	27.6	0.6	2.3	29	26.8	27	28
Sm 147	6.43	0.16	2.5	6.6	6.29	6.3	6.3
Eu 153	1.92	0.04	2.2	1.92	1.80	1.91	1.85
Gd 158	6.36	0.18	2.8	6.5	6.15	6.5	6.7
Dy 162	6.01	0.15	2.6	6.5	6.13	6.0	6.2
Ho 165	1.21	0.03	2.6	1.31	1.19	1.20	1.15
Er 166	3.43	0.09	2.7	3.6	3.48	3.3	3.8
Yb 174	3.19	0.09	2.9	3.5	3.17	3.2	3.2
Lu 175	0.48	0.02	3.9	0.51	0.48	0.47	0.54
Hf 178	4.61	0.13	2.7	5.00	4.8	4.5	n.a.
Ta 181	0.78	0.02	3.0	0.78	0.72	0.63	n.a.
Pb 208	11.61	0.33	2.8	11.50	11.0	10.9	9.7
Th 232	5.67	0.15	2.7	6.10	5.55	5.5	5.8
U 238	1.75	0.06	3.2	1.73	1.6	1.70	1.7
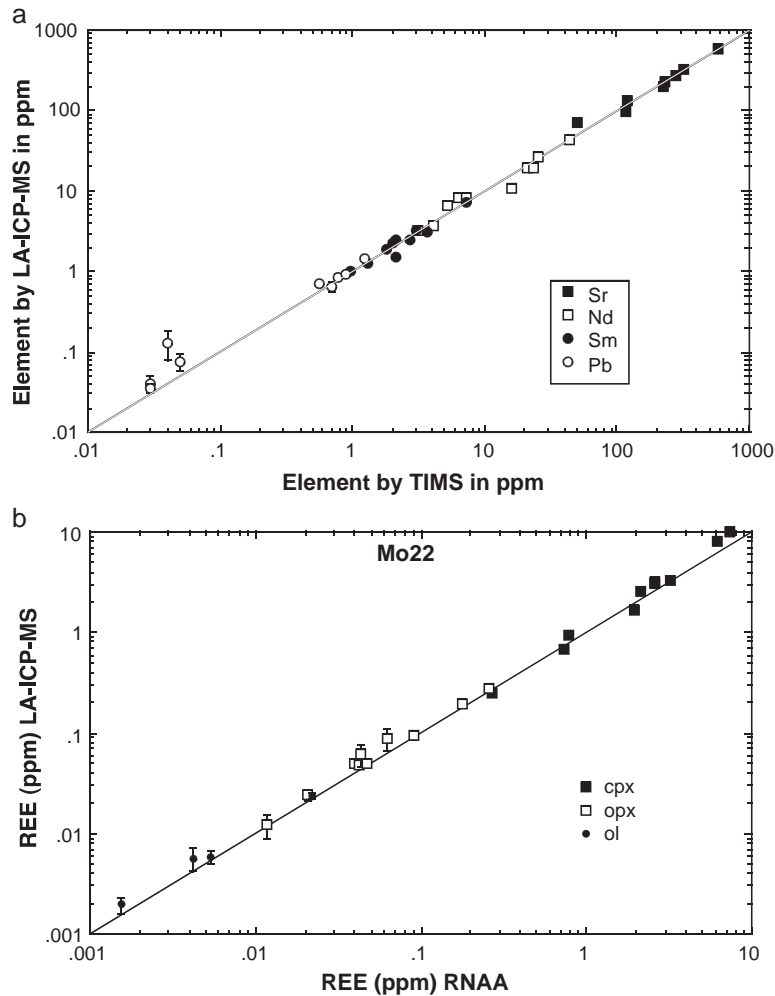
Fig. 1. a) Comparison between the present LA-ICP-MS determinations on Sr, Nd, Sm, and Pb in clinopyroxene and results previously obtained by TIMS on mineral separates by Witt-Eickschen and Kramm (1997) and Witt-Eickschen et al. (2003). b) REE in cpx, opx and ol from Mo22: comparison of the results of this study (LA-ICP-MS) with those of Stosch (1982) using RNAA on hand-picked mineral separates. Agreement is excellent, extending over four orders of magnitude in REE abundances.

Cameca ims-4f ion microprobe (Department of Geology and Geophysics in Edinburgh, U.K.). Detailed information about the analytical conditions, corrections and quantification are given in Witt-Eickschen and Harte (1994).

The REEs in all four phases of one of the xenoliths in our suite, Mo22, have been determined previously by Stosch (1982), using radiochemical neutron activation on hand-picked, HF-washed mineral separates. Agreement of our data with this earlier work is excellent, as shown in Fig. 1b.

3. The xenolith samples

The 16 xenoliths used in this study are typical examples of spinel-lherzolite xenoliths hosted in alkali basalts. Fourteen xenoliths are from Quaternary maar eruptions in the West Eifel, Germany (DW: Dreiser Weiher, MM: Meerfelder Maar), and these were supplemented by one sample each from Cenozoic basalts of the Rother Berg volcano (Westerwald/Germany, RB1189) and the Shavaryn Tsaram volcano (Tariat Depression/Mongolia: Mo22). The petrological, geo-

chemical and Sr–Nd–Pb isotope characteristics for most of the samples have been presented and discussed elsewhere (e.g., Press et al., 1986; Stosch et al., 1986; Witt-Eickschen and Kramm, 1998; Witt-Eickschen et al., 2003). The modal mineralogy and several important geochemical and mineralogical attributes including calculated temperatures of equilibration are listed in Table 2, and the major element mineral compositions are presented in Table 3a–e.

The xenoliths were selected for the major-element homogeneity of all their minerals, as revealed by the previous work. There is no exsolution in the mineral grains detectable either by optical microscope or under the electron microprobe. All grains analysed by LA-ICP-MS were previously checked for zoning by electron microprobe, either by core–rim analyses or full traverses. In addition, trace-element homogeneity was addressed directly by LA-ICP-MS traverses using a 29 μm spot over one selected grain in each of the following samples:

MM1240 (cpx), MM1260 (cpx, opx), MM1213 (cpx, ol), DWv2 (cpx, ol), DW1283 (cpx), DW1342 (cpx, opx), DW599 (cpx, opx), RB1189 (cpx), Mo22 (cpx), MM110 (amph), DW1284 (cpx, opx), DW582 (cpx), MM1278 (cpx, opx), DW210 (cpx, opx, ol), DW211 (cpx, ol).

The xenoliths were also chosen to cover as large a range of equilibration temperatures as possible. Equilibration temperatures were calculated using two formulations of the orthopyroxene–clinopyroxene Ca–Mg exchange equilibrium, from Brey and Köhler (1990). The first utilizes only the composition of the opx:

$$T_{(opx)} = \frac{6425 + 26.4P}{-\ln\left(N_{Ca}^{opx}\right) + 1.843} \tag{1}$$

where P is pressure in kbars, and N_{Ca}^{opx} is the number of Ca cations in opx per formula unit of six oxygens. The second formulation uses both opx and cpx compositions:

$$T_{(cpx/opx)} = \frac{23664 + (24.9 + 126.3Fe\#^{cpx})P}{13.38 + (\ln KD^*)^2 + 11.59Fe\#^{opx}} \tag{2}$$

where

$$KD^* = \frac{\left(1 - N_{Ca}^{cpx}/\left(1 - N_{Na}^{cpx}\right)\right)}{\left(1 - N_{Ca}^{opx}/\left(1 - N_{Na}^{opx}\right)\right)}$$

and $Fe\#^{cpx}$ and $Fe\#^{opx}$ is molar Fe/(Fe+Mg) in cpx and opx, respectively.

There is unfortunately no precise way of calculating pressures in spinel lherzolites; available pres-

Table 2
Summary of the petrography and geochemistry of the xenoliths

Xenolith	Mode					T(K) opx 1.5 GPa[1]	T(K) cpx/opx 1.5 GPa[2]	X_{Mg} olivine	Cr# spinel	N_{Na} cpx	Nd (cpx/CI)$_N$[3]	$\Delta\log(fO_2)$ (QFM)[4]
	ol	opx	cpx	sp	amph							
MM1240	80	18	2	<1	–	1491	1508	0.919	0.46	0.050	5.1	−0.39
MM1260	73	20	5	2	–	1481	1500	0.917	0.42	0.047	1.8	−0.27
MM1213	84	13	2	1	–	1478	1513	0.921	0.45	0.051	3.2	−0.53
DWv2	87	9	3	1	–	1462	1519	0.908	0.34	0.073	8.0	−0.87
DW1283	82	13	5	<1	–	1453	1508	0.916	0.37	0.071	6.9	−0.54
DW1342	86	8	3	2		1443	1484	0.916	0.41	0.093	17.3	−0.46
DW599	70	19	10	1	–	1394	1473	0.913	0.13	0.103	6.9	−0.36
RB1189	48	37	13	2	–	1339	1442	0.917	0.24	0.083	13.6	0.01
Mo22	63	21	14	3	–	1325	1407	0.896	0.11	0.108	17.2	−1.02
MM110*	75	16	4	<1	5	1259	1289	0.914	0.44	0.113	90	−0.48
MM766*	60	33	2	2	2	1253	1301	0.917	0.28	0.077	41	−0.08
DW1284**	63	26	6	3	1	1162	1179	0.915	0.20	0.062	56	0.40
DW582**	68	22	6	1	3	1159	1223	0.920	0.28	0.066	42	0.25
MM1278*	62	24	8	2	3	1149	1243	0.914	0.20	0.052	24	0.36
DW210**	63	26	7	2	2	1149	1183	0.917	0.20	0.065	22	0.62
DW211*	80	11	4	3	3	1145	1230	0.916	0.47	0.088	91	0.18

*Amphibole preserved. **Melt pools after amphibole. [1] Eq. (1) in the text; [2] Eq. (2) in the text. Both from Brey and Köhler (1990). [3] Chondrite normalized. [4] Calculated using the method of O'Neill and Wall (1987), assuming $T_{(opx/1.5\ GPa)}$ and 1.5 GPa, with their $\Delta G°(4)$ changed to $-14{,}540 + 71.44T - 8.9T\ln(T) - 37.5\ P$.

Table 3

	MM1240		MM1260		MM1213		DW-v2		DW1283		DW1342		DW599		RB1189	
a. Major and trace element analyses of clinopyroxenes																
wt.%																
SiO_2	53.55		52.08		53.37		51.24		53.28		53.10		51.46		52.34	
TiO_2	0.15		0.12		0.07		0.64		0.17		0.44		0.38		0.49	
Al_2O_3	4.33		4.61		4.30		5.68		5.09		5.04		7.42		6.38	
Cr_2O_3	1.63		1.55		1.67		1.69		1.72		1.71		1.11		1.25	
FeO	3.11		3.24		3.01		3.44		3.17		3.10		3.32		3.21	
MnO	0.10		0.10		0.10		0.11		0.09		0.12		0.10		0.00	
NiO	0.07		0.07		0.07		0.06		0.07		0.06		0.06		0.06	
MgO	18.77		18.41		18.61		17.68		18.06		17.40		16.72		16.29	
CaO	18.68		18.49		18.44		17.20		18.09		18.15		17.92		19.04	
Na_2O	0.72		0.66		0.73		1.03		1.03		1.34		1.47		1.19	
Total	101.09		99.33		100.36		98.78		100.78		100.46		99.96		100.25	
N =	5	s.d.	2	s.d.	2	s.d.	5	s.d.	8	s.d.	3	s.d.	3	s.d.	4	s.d.
ppm																
P	38	2	29	2	39	2	24	3	28	3	51	3	50	2	53	7
Sc	38.0	0.1	36.5	0.1	37.1	0.2	34.6	0.2	37.1	0.2	45.7	0.1	48.5	0.4	53.2	0.6
Ti	893	5	727	3	426	1	3821	40	1024	15	2612	47	2303	18	2916	211
V	167	1	161	0	145	0	200	2	200	4	164	4	222	2	240	6
Cr	11,160	64	10,634	15	11,407	85	11,595	235	11,786	632	11,713	32	7612	264	8568	565
Co	33.1	0.3	33.5	0.2	32.4	0.2	31.1	0.2	31.7	0.5	30.8	0.1	28.8	0.6	27.2	0.9
Ni	548	4	542	1	534	3	477	3	517	6	493	1	448	6	452	13
Ga	3.09	0.03	3.28	0.07	2.83	0.01	6.12	0.07	3.91	0.11	3.93	0.16	5.25	0.17	4.92	0.23
Sr	37.1	0.1	16.1	0.2	30.7	0.1	52.0	0.4	68.2	9.8	99.5	2.2	63.0	0.3	100.9	0.3
Y	3.47	0.05	5.38	0.00	6.29	0.09	7.80	0.10	6.03	0.27	9.23	0.03	16.14	0.11	12.78	0.11
Zr90	6.44	0.13	2.54	0.00	2.72	0.02	13.56	0.07	12.69	0.84	23.84	1.13	24.40	0.12	21.27	0.69
Zr91	6.51	0.12	2.50	0.06	2.73	0.10	13.41	0.14	12.64	0.89	23.75	1.08	24.31	0.02	21.27	0.69
ppb																
Nb	164	13	121	2	208	7	199	10	786	46	443	77	267	8	1338	39
Ba	124	8	61	15	151	3	89	19	339	266	1185	591	42	2	601	505
La	726	6	219	2	773	24	1029	18	2375	270	2679	81	832	11	5264	86
Ce	2644	15	749	18	2221	4	3738	44	5146	637	9600	275	2924	24	10,784	275
Nd	2411	28	854	36	1502	13	3769	51	3278	278	8216	295	3263	38	6440	137
Sm	689	22	370	12	491	4	1252	22	973	35	2221	55	1339	25	2015	58
Eu	227	7	164	6	202	7	456	11	341	11	748	23	561	2	729	24
Gd	677	13	635	6	787	1	1525	36	1058	48	2249	35	2024	21	2435	37
Dy	595	12	862	1	1055	14	1507	61	974	38	1790	15	2505	23	2391	70
Ho	123	2	187	3	227	5	283	10	188	9	328	5	547	3	474	4
Er	363	13	546	5	637	16	707	24	510	23	822	10	1579	19	1272	25
Yb	329	8	484	5	567	13	494	19	435	23	601	3	1414	8	1006	17
Lu	48	1	73	2	75	4	63	3	64	4	81	1	212	4	140	4
Hf	195	9	119	4	88	10	610	18	338	17	842	29	715	19	712	87
Ta	11	1	4	1	13	1	21	1	77	8	42	6	20	2	83	4
Pb	117	48	312	101	46	7	40	10	291	450	76	18	24	11	72	2
Th	10.8	1.4	5.8	1.8	21.7	1.9	16.5	1.3	128.5	7.6	44.4	8.6	22.1	0.9	308.2	13.1
U	1.9	0.7	1.6	1.0	3.8	0.0	2.6	0.5	22.8	1.7	9.0	2.6	6.1	0.4	54.7	2.9
b. Major and trace element analyses of orthopyroxenes																
wt.%																
SiO_2	55.82		54.55		55.42		53.91		56.06		55.70		53.95		55.06	
TiO_2	0.08		0.06		0.04		0.29		0.08		0.14		0.14		0.16	
Al_2O_3	3.79		4.10		3.83		4.70		4.29		3.84		6.03		4.44	
Cr_2O_3	1.19		1.13		1.17		1.10		1.11		1.06		0.61		0.74	

MO22		MM110		MM766		DW1284		DW582		MM1278		DW210		DW211	
51.85		52.84		53.22		52.96		53.37		53.18		53.55		53.57	
0.51		0.09		0.07		0.04		0.05		0.06		0.06		0.04	
6.93		4.34		4.34		3.75		3.42		3.73		3.82		2.85	
0.86		1.49		0.76		0.73		0.82		0.59		0.75		1.16	
3.58		2.60		2.55		2.51		2.43		2.62		2.39		2.37	
0.00		0.10		0.09		0.08		0.06		0.07		0.08		0.07	
0.05		0.04		0.05		0.05		0.05		0.04		0.05		0.04	
15.45		15.79		16.63		16.59		16.90		16.96		16.45		16.35	
18.70		19.98		20.85		22.12		21.77		21.91		22.17		20.99	
1.53		1.59		1.10		0.88		0.94		0.74		0.92		1.24	
99.46		98.87		99.65		99.69		99.79		99.89		100.25		98.68	
6	s.d.	2	s.d.	2	s.d.	3	s.d.	2	s.d.	4	s.d.	6	s.d.	5	s.d.
148	20	141	9	103	6	50	3	50	3	46	3	43	5	62	4
53.2	0.7	61	1.3	68.5	2.2	70.9	0.6	72.8	0.1	67.9	0.3	67.7	1.3	73.8	1.4
3059	37	565	28	415	1	248	2	273	0	366	4	382	59	243	6
254	1	187	3	192	0	124	1	185	1	200	0	209	10	206	4
5864	125	10,168	256	5217	200	4997	636	5608	93	4016	22	5129	884	7947	192
26.9	0.1	21.3	0.2	24.8	1.1	22.4	1.6	21.5	0.1	20.3	0.5	21.9	2.3	20.8	1.0
411	3	353	1	425	55	375	21	358	2	325	7	368	25	348	18
5.53	0.13	4.39	0.11	2.69	0.08	2.28	0.12	2.25	0.02	2.30	0.03	2.41	0.38	3.45	0.07
136.3	4.1	315.9	0.6	275.3	4.7	327.6	5.5	225.0	6.5	200.1	3.1	176.3	24.8	581.5	34.8
19.07	0.41	20.18	0.71	8.90	0.62	7.26	0.06	9.22	0.11	8.09	0.16	8.30	0.11	13.61	0.32
65.22	7.03	51.55	1.16	12.24	1.26	9.38	0.15	14.30	0.02	13.14	0.17	7.01	3.35	25.33	0.68
65.11	6.94	51.56	1.08	12.02	1.19	9.18	0.04	14.47	0.01	13.30	0.11	7.05	3.34	25.22	0.73
1160	58	1444	97	1072	57	1585	232	1240	6	528	13	655	92	824	41
97	2	342	8	320	26	312	48	242	9	272	17	1588	2185	447	65
3202	127	22,081	488	18,489	438	19,649	1345	15,566	659	20,910	237	15,443	1346	32,746	4339
9823	394	68,519	1953	54,224	1298	54,939	2964	43,266	1126	39,852	1463	31,703	1795	83,576	8939
8160	511	42,661	1483	19,318	839	26,490	1112	19,763	313	11,300	628	10,537	543	43,266	2983
2546	152	8485	394	2509	119	3222	125	3099	70	1472	98	1517	122	7405	368
943	45	2364	118	700	40	821	30	870	16	394	14	436	28	2112	97
3019	113	6271	272	1868	152	1709	37	2082	51	1185	36	1223	87	4748	170
3301	90	4134	105	1579	134	1170	26	1598	19	1285	7	1298	28	2897	91
677	13	715	19	311	25	243	10	312	0	296	0	286	4	494	12
1926	42	1850	51	894	76	744	10	860	12	913	0	889	25	1253	29
1688	21	1460	23	832	43	766	4	812	25	926	14	883	35	1050	18
246	3	205	3	125	16	119	4	123	3	135	2	136	6	151	2
1289	111	957	45	156	20	144	7	118	0	180	4	70	11	200	5
164	22	139	16	115	12	209	30	147	2	136	18	66	7	81	4
168	25	476	4	652	93	936	62	694	31	1459	32	1035	95	855	50
		1153.9	82.4	505.1	35.7	1716.7	138.9	1826.1	7.6	2197.1	5.1	1477.7	58.1	2060.8	184.5
		221.5	22.2	77.8	0.4	329.1	27.7	278.5	4.9	480.2	15.4	337.5	7.2	381.5	35.7
54.59		55.64		55.98		55.79		56.29		55.89		55.57		56.93	
0.15		0.02		0.02		0.01		0.01		0.02		0.02		0.01	
5.55		2.44		3.44		3.15		2.70		3.33		3.29		1.98	
0.48		0.53		0.46		0.38		0.41		0.35		0.34		0.36	

Table 3 (*continued*)

	MM1240		MM1260		MM1213		DW-v2		DW1283		DW1342		DW599		RB1189	
b. Major and trace element analyses of orthopyroxenes																
wt.%																
FeO	5.08		5.22		4.98		5.67		5.21		5.11		5.64		5.35	
MnO	0.12		0.12		0.12		0.13		0.12		0.09		0.12		0.00	
NiO	0.13		0.13		0.12		0.11		0.13		0.12		0.12		0.11	
MgO	32.77		32.50		32.86		31.91		32.54		32.33		32.63		33.31	
CaO	1.76		1.69		1.68		1.58		1.57		1.49		1.27		1.05	
Na$_2$O	0.10		0.09		0.10		0.15		0.14		0.22		0.17		0.00	
Total	100.85		99.59		100.32		99.54		101.24		100.11		100.67		100.23	
N =	3	s.d.	5	s.d.	7	s.d.	3	s.d.	3	s.d.	2	s.d.	4	s.d.	7	s.d.
ppm																
P	33	1	27	2	33	2	25	2	22	2	24	1	37	2	24	2
Sc	21.0	0.2	20.4	0.1	20.0	0.2	17.4	0.2	17.9	0.0	20.1	0.0	20.8	0.2	19.4	0.8
Ti	486	2	385	3	227	4	1721	9	485	4	864	28	820	7	972	59
V	99	2	96	2	83	1	108	1	107	3	83	1	110	1	108	5
Cr	8123	133	7760	138	7980	131	7526	59	7614	114	7272	71	4205	57	5092	193
Co	69.8	1.0	69.5	0.9	65.6	0.4	62.8	0.4	67.2	0.5	66.6	0.1	66.9	0.4	60.4	3.1
Ni	1043	14	1011	12	978	4	878	7	983	4	959	2	917	5	866	43
Ga	3.41	0.04	3.58	0.10	3.04	0.04	5.90	0.04	3.96	0.06	3.85	0.03	5.15	0.05	4.71	0.19
Sr	0.512	0.041	0.198	0.005	0.382	0.012	0.998	0.008	0.898	0.201	0.917	0.038	0.529	0.008	0.633	0.148
Y	0.531	0.004	0.806	0.019	0.940	0.021	0.667	0.020	0.805	0.047	1.154	0.010	1.695	0.008	1.188	0.028
Zr90	1.42	0.05	0.55	0.01	0.58	0.01	2.33	0.02	2.21	0.12	3.28	0.00	3.06	0.03	2.25	0.06
Zr91	1.35	0.03	0.53	0.04	0.56	0.04	2.29	0.04	2.19	0.13	3.28	0.08	3.09	0.09	2.26	0.05
ppb																
Nb	73	2	62	3	78	5	60	2	168	39	92	7	40	2	156	5
Ba	4	1	4	1	6	1	4	0	176	288	4	2	2	1	9	7
La	9	2	2	1	11	2	12	1	37	16	23	0	5	1	31	7
Ce	50	1	13	2	39	1	60	3	87	14	118	4	29	1	94	28
Nd	71	4	21	6	43	4	91	2	84	9	163	7	54	2	86	11
Sm	33	7	15	5	18	4	47	3	40	3	72	2	39	2	46	4
Eu	13	1	9	2	11	1	22	1	16	1	36	2	21	2	22	2
Gd	45	7	43	5	51	4	90	6	64	3	123	0	94	5	92	7
Dy	74	6	99	8	116	5	151	6	100	1	171	10	203	9	161	8
Ho	19	1	26	1	33	2	33	1	24	1	39	0	55	2	42	1
Er	64	6	98	5	108	6	109	4	83	6	127	4	204	3	145	4
Yb	97	6	135	6	153	7	119	5	106	13	136	2	290	3	191	5
Lu	17	1	24	2	26	1	19	1	19	3	27	0	52	2	33	3
Hf	41	2	22	3	17	2	95	3	50	6	107	0	87	6	69	4
Ta	<1		<1		2	1	1	1	7	2	3	0	2	1	4	1
Pb	111	39	405	147	42	9	27	6	98	33	29	1	16	5	19	4
Th	<1		<1		0.7	0.4	0.5	0.1	7.5	10.1	1.8	0.2	0.5	0.5	4.44	0.7
U	<1		<1		<1		<1		2.5	1.6	1.0	0.1	− 0.4	0.4	2.1	0.4.
c. Major and trace element analyses of olivines																
wt.%																
SiO$_2$	41.80		40.73		41.91		40.43		41.44		41.34		40.53		40.58	
TiO$_2$	0.00		0.00		0.00		0.01		0.00		0.01		0.01		0.01	
Al$_2$O$_3$	0.05		0.07		0.05		0.06		0.06		0.00		0.05		0.00	
Cr$_2$O$_3$	0.08		0.07		0.07		0.06		0.08		0.06		0.03		0.03	
FeO	8.04		8.11		7.78		8.96		8.24		8.17		8.61		8.09	
MnO	0.12		0.13		0.12		0.13		0.12		0.13		0.14		0.00	
NiO	0.42		0.41		0.42		0.38		0.40		0.41		0.40		0.41	
MgO	51.20		50.51		50.79		49.86		50.26		50.16		50.77		50.41	

MO22		MM110		MM766		DW1284		DW582		MM1278		DW210		DW211	
6.17		5.28		5.30		5.40		5.17		5.55		5.48		5.25	
0.13		0.15		0.13		0.13		0.14		0.14		0.14		0.14	
0.11		0.11		0.10		0.11		0.11		0.10		0.10		0.09	
31.75		33.46		33.85		34.13		34.70		34.42		34.51		34.62	
0.99		0.74		0.74		0.48		0.48		0.45		0.45		0.44	
0.00		0.09		0.06		0.03		0.04		0.03		0.03		0.05	
99.92		98.46		100.09		99.62		100.04		100.27		99.92		99.86	
4	s.d.	6	s.d.	2	s.d.	3	s.d.	2	s.d.	3	s.d.	1	s.d.	5	s.d.
40	1	34	4	36	2	38	2	38	1	25	2	24		22	4
17.7	0.2	15.9	2.5	17.8	1.1	17.1	0.5	16.0	0.8	17.1	0.5	14.5		11.6	1.4
902	8	120	11	142	3	73	0	84	4	100	3	100		70	6
104	1	59	8	81	8	49	1	66	3	80	4	71		47	5
3257	72	3618	391	3136	833	2623	269	2789	120	2425	95	2305		2476	321
69.0	1.9	66.9	11.3	61.8	6.4	63.9	0.7	63.4	3.7	61.0	3.0	58.0		54.0	6.4
902	25	870	151	801	80	847	18	839	54	769	40	754		705	85
4.99	0.08	3.62	0.45	3.03	0.49	2.65	0.06	2.45	0.12	2.92	0.14	2.29		2.65	0.32
0.636	0.172	0.636	0.057	0.464	0.006	0.408	0.141	0.225	0.054	0.285	0.013	0.208		0.596	0.026
1.513	0.014	1.160	0.151	0.695	0.029	0.440	0.006	0.570	0.023	0.491	0.007	0.440		0.687	0.062
6.03	0.58	1.99	0.31	0.95	0.02	0.47	0.01	0.60	0.00	0.63	0.00	0.52		0.73	0.05
5.97	0.64	2.02	0.30	0.97	0.01	0.42	0.04	0.64	0.04	0.64	0.02	0.51		0.74	0.05
54	19	77	12	69	5	74	27	59	4	46	1	34		48	4
1	1	3	1	3	1	3	1	2	1	4600	937	3		13	23
12	3	31	4	29	1	29	9	22	0	31	1	21		35	2
61	15	170	21	146	3	134	39	96	5	105	3	74		153	8
87	21	215	43	106	11	105	27	77	4	60	8	36		163	15
50	5	84	10	32	3	27	2	23	4	11	4	12		55	3
24	3	33	7	13	0	11	1	11	0	6	1	6		23	3
94	9	116	18	43	2	28	2	37	0	20	1	16		68	5
193	3	161	23	83	4	43	2	63	3	47	2	51		90	6
49	1	39	5	24	0	13	3	17	0	15	1	13		22	1
186	5	138	16	85	5	60	8	71	1	72	3	65		83	10
275	2	199	20	165	1	127	5	134	10	142	7	121		134	11
49	2	36	4	31	5	25	1	27	0	28	1	26		24	3
98	7	26	11	13	3	7	1	6	1	9	1	3		6	1
3	2	2	0	3	1	2	2	2	0	2	1	1		1	0
52	24	20	9	14	8	7	12	96	11	58	31	65		66	20
nd		6.5	0.7	2.8	2.5	12.0	2.5	10.6	0.8	19.9	2.0	15.5		13.6	1.5
nd		4.2	0.5	2.3	0.3	8.2	1.3	5.7	0.8	13.0	1.4	5.8		6.7	0.3
40.85		40.33		41.16		40.75		40.92		40.88		40.70		40.72	
0.01		0.00		0.00		0.00		0.00		0.00		0.00		0.00	
0.00		0.01		0.01		0.01		0.01		0.01		0.01		0.01	
0.02		0.02		0.01		0.01		0.01		0.01		0.01		0.01	
10.05		8.26		8.08		8.35		7.87		8.56		8.17		8.19	
0.00		0.15		0.12		0.13		0.12		0.13		0.13		0.16	
0.39		0.39		0.45		0.46		0.41		0.38		0.43		0.44	
48.80		49.53		50.04		50.66		51.08		50.90		50.68		50.10	

Table 3 (*continued*)

	MM1240		MM1260		MM1213		DW-v2		DW1283		DW1342		DW599		RB1189	
c. Major and trace element analyses of olivines																
wt.%																
CaO	0.16		0.17		0.16		0.15		0.16		0.12		0.12		0.11	
Total	101.87		100.19		101.31		100.04		100.76		100.39		100.65		99.64	
N =	3	s.d.	3	s.d.	4	s.d.	2	s.d.	3	s.d.	4	s.d.	5	s.d.	3	s.d.
ppm																
P	69	1	32	2	72	3	38	2	34	3	20	0	69	9	64	4
Sc	4.8	0.0	4.5	0.0	4.6	0.1	3.7	0.1	3.8	0.1	4.4	0.0	4.0	0.3	3.9	0.1
Ti	25.8	0.5	27.6	0.1	13.0	0.4	80.1	5.2	24.1	1.1	52.7	1.6	34.2	1.8	52.6	1.7
V	7.1	0.5	6.7	1.5	5.9	0.2	7.1	0.0	7.5	0.3	5.8	0.1	5.7	0.2	6.2	0.2
Cr	556	78	485	0	503	28	423	2	579	85	423	10	197	8	238	8.5
Co	153	1	152	5	151	2	140	1	145	1	150	1	150	9	148	6
Ni	3292	21	3247	0	3329	47	2949	12	3156	18	3222	12	3125	103	3218	121
ppb																
Sr	8.7	7.3	16.8	2.2	7.3	2.7	7.0	0.3	8.9	1.2	14.3	4.6	4.9	3.6	13.8	10.4
Y	32.5	3.7	51.9	6.0	51.1	2.7	51.0	0.9	40.5	1.2	58.9	3.2	76.4	2.9	55.6	2.6
Zr90	48.5	13.4	48.5	1.1	22.8	7.2	55.3	2.8	56.0	2.3	89.5	4.2	46.1	8.0	53.6	2.0
Zr91	48.7	14.5	53.2	6.1	25.2	9.5	52.2	9.3	54.7	12.0	116.6	9.1	–		46.8	12.6
Nb	5.8	0.5	4.4	9.5	5.8	1.6	3.5	0.3	7.9	0.3	4.9	0.5	2.0	0.4	9.8	1.8
Ho	0.9	0.7	1.5	0.3	1.4	0.6	1.1	0.3	1.2	0.5	1.9	0.6	13.9	14.4	1.3	0.1
Er	4.2	2.2	9.6	0.2	8.0	0.8	6.6	1.5	4.7	0.9	7.8	1.2	11.6	7.6	8.5	1.2
Yb	9.9	2.4	14.9	1.8	13.9	1.1	12.5	0.4	11.5	1.5	15.1	1.2	12.9	14.4	19.2	1.7
Lu	1.2	0.8	3.1	1.3	2.7	0.8	2.9	0.5	2.3	0.3	3.8	0.8	3.6	3.4	4.1	0.4
Pb	208.1	20.6	338.4	116.3	55.2	11.6	11.7	2.2	26.5	11.7	67.3	39.5	212.2	52.4	41.4	6.5
d. Major and trace element analyses of spinels																
wt.%																
TiO$_2$	0.36		0.26		0.15		1.03		0.26		0.75		0.19		0.52	
Al$_2$O$_3$	29.71		32.35		30.43		37.46		35.55		32.63		54.51		45.42	
Cr$_2$O$_3$	37.58		34.59		37.27		28.91		31.22		33.97		12.61		21.33	
FeO	14.16		14.23		13.78		13.32		12.83		13.76		11.16		12.31	
MnO	0.17		0.13		0.18		0.16		0.11		0.16		0.10		0.00	
NiO	0.25		0.23		0.24		0.27		0.26		0.27		0.35		0.33	
MgO	17.65		17.97		17.34		18.67		18.37		18.18		21.07		20.45	
Total	99.87		99.75		99.41		99.79		98.61		99.71		99.99		100.36	
N =	3	s.d.	4	s.d.	3	s.d.	2	s.d.	4	s.d.	3	s.d.	2	s.d.	4	s.d.
ppm																
Sc	3.8	0.1	3.7	0.1	3.5	0.3	2	0.1	2.5	0.1	3.0	0.1	1.0	0.0	1.92	0.02
Ti	2105	3	1600	43	959	36	5637	94	1605	30	4336	89	1103	6	2742	326
V	877	9	806	2	739	23	761	10	778	2	687	5	428	6	717	11
Cr	267,012	1279	246,656	2631	265,390	4608	207,403	3724	227,315	4809	243,155	7333	92,190	1704	159,691	4721
Co	220	5	208	2	213	5	192	3	201	9	215	4	205	5	213	6
Ni	2110	36	2279	31	2066	50	2280	79	2269	82	2297	33	3181	40	2779	131
Ga	46.4	1.0	50.4	1.4	43.3	1.9	83.6	2.6	55.1	2.2	58.3	0.6	75.4	0.7	79.9	4.6
ppb																
Sr	61.3	2.3	125.8	138.2	47.5	10.5	143.7	125.7	42.0	6.4	75.5	12.2	26.3	1.3	69.0	16.8
Y	9.1	3.6	8.2	4.5	6.4	1.4	1.7	1.8	6.5	1.0	15.2	4.3	3.4	2.0	6.5	2.8

MO22		MM110		MM766		DW1284		DW582		MM1278		DW210		DW211	
0.09		0.05		0.07		0.06		0.05		0.05		0.04		0.05	
100.20		98.73		99.93		100.43		100.48		100.90		100.16		99.67	
10	s.d.	4	s.d.	4	s.d.	3	s.d.	12	s.d.	2	s.d.	4	s.d.	7	s.d.
99	3	141	21	122	28	103	66	105	47	58	1	62	18	164	27
3.7	0.1	3.2	0.1	3.0	0.0	2.8	0.1	2.7	0.1	3.1	0.0	2.3	0.0	3.1	0.0
32.7	1.8	5.5	0.1	6.1	0.3	3.3	0.3	4.0	0.2	4.0	0.1	3.6	0.2	4.3	0.1
4.8	0.3	1.9	0.0	2.6	0.1	1.5	0.0	1.9	0.1	2.0	0.0	1.7	0.0	2.3	0.0
147	34	115	1	88	2	60	2	65	1	52	3	42	1	93	2
156	1	148	2	152	3	154	3	145	2	147	1	155	4	160	2
3036	8	3090	49	3508	73	3645	76	3238	43	2984	26	3402	95	3457	54
23.7	49.3	22.2	13.5	138.0	246.5	4.3	1.3	19.8	36.2	9.4	8.8	22.9	23.4	31.3	59.9
64.8	5.6	37.5	2.1	22.1	6.2	18.5	2.3	16.8	2.1	14.9	2.2	12.0	0.9	29.1	2.0
91.6	18.9	43.7	13.1	–		11.2	2.9	15.0	1.7	13.6	1.6	11.3	2.1	28.1	1.8
94.3	18.6	48.2	18.3	–		–		11.7	10.2	16.2	6.2	15.7	6.7	34.7	3.2
2.3	0.6	19.6	7.3	13.1	4.8	10.5	0.5	13.2	3.4	3.3	0.4	9.7	12.1	10.0	0.8
1.9	0.4	1.3	0.3	0.5	0.7	0.4	0.3	0.2	0.3	0.7	0.1	0.2	0.3	0.9	0.3
10.4	1.7	4.3	1.1	4.3	2.3	3.4	1.2	2.3	0.5	2.1	0.7	2.3	0.7	4.5	0.7
23.5	1.9	15.4	2.6	10.6	0.5	9.9	2.0	8.5	1.9	9.1	0.3	7.7	0.8	12.3	1.3
5.8	0.9	4.2	0.2	3.2	0.2	2.0	0.7	2.1	0.5	3.0	0.8	2.0	0.4	3.1	0.7
30.5	20.4	39.1	5.0	52.3	42.2	39.8	17.5	92.1	51.5	75.2	8.0	65.3	8.8	115.6	27.6
0.20		0.09		0.05		0.02		0.03		0.03		0.03		0.08	
57.85		31.05		42.69		48.89		42.52		48.75		47.48		28.42	
10.40		35.79		24.47		17.76		24.90		17.86		18.17		38.09	
10.68		15.22		13.07		12.98		13.48		13.26		13.06		17.21	
–		0.21		0.19		0.12		0.15		0.12		0.11		0.18	
0.46		0.20		0.33		0.35		0.27		0.33		0.35		0.20	
21.38		16.14		18.80		19.74		18.87		19.53		19.66		15.91	
100.51		98.70		99.60		99.86		100.23		99.89		98.86		100.06	
4	s.d.	1	s.d.	2	s.d.	3	s.d.	2	s.d.	2	s.d.	3	s.d.	6	s.d.
0.8	0.0	1.9		1.3	0.0	0.9	0.0	1.2	0.0	0.9	0.1	0.8	0.0	2.2	0.1
1211	16	646		345	4	157	1	224	6	164	12	212	8	490	17
428	6	701		702	11	344	3	622	6	533	25	614	23	983	33
79,511	840	260,459		191,407	7466	134,988	5451	174,354	1704	114,086	6302	136,829	7528	276,158	9769
243	4	264		278	3	266	0	279	5	253	1	305	15	288	10
3591	64	1558		2447	22	3116	75	2431	40	2743	60	3259	77	1659	49
100.5	2.3	68.6		68.0	0.6	62.2	0.8	56.4	0.7	59.3	0.3	62.9	3.0	73.5	3.5
14.8	2.5	87.6		26.1	0.1	20.5	4.6	35.6	1.3	217.8	272.7	33.1	11.2	378.5	698.8
5.7	2.2	7.8		8.2	5.1	13.7	3.7	1.2	2.0	10.5	9.1	5.3	3.8	18.3	17.9

Table 3 (continued)

	MM110		MM766		MM1266		DW211	
e. Major and trace element analyses of amphiboles								
wt.%								
SiO_2	44.20		44.28		43.75		44.49	
TiO_2	0.47		0.52		0.27		0.36	
Al_2O_3	13.22		14.68		15.03		13.35	
Cr_2O_3	2.34		1.93		1.43		2.03	
FeO	3.74		3.73		4.15		4.06	
MnO	0.02		0.01		0.04		0.00	
NiO			0.12		0.12		0.12	
MgO	18.10		17.92		17.74		18.24	
CaO	10.63		11.20		11.26		10.64	
Na_2O	3.42		3.08		3.06		3.28	
K_2O	1.10		1.21		1.10		0.91	
Total	97.24		98.68		97.95		97.48	
$N=$	8	s.d.	3	s.d.	3	s.d	5	s.d.
ppm								
P	262	32	290	55	174	10	228	12
Sc	50.4	0.9	58.5	0.8	56.6	0.2	56.0	1.2
Ti	2922	132	2773	30	1804	21	1776	78
V	297	3	468	34	407	3	386	7
Cr	15,785	303	17,847	5206	8737	202	13,933	155
Co	37.4	0.3	44.2	6.5	42.0	0.3	38.5	0.9
Ni	854	10	951	64	965	3	910	28
Ga	33.6	2.9	27.5	4.3	7.4	0.1	18.3	6.7
Rb	12.3	1.5	17.1	2.6	24.4	0.4	7.8	0.7
Sr	550.9	4.5	637.1	11.0	473.4	29.4	905.4	44.0
Y	20.5	0.7	14.0	0.3	15.7	0.5	20.2	0.6
Zr90	64.1	4.3	25.1	0.3	19.5	0.2	41.4	1.3
Zr91	64.0	4.3	25.1	0.5	19.3	0.2	41.7	0.9
Nb	157.2	11.3	179.4	4.7	89.4	2.7	143.5	2.3
Ba	260	32	379	109	648	52	257	31
La	28.5	1.5	30.4	3.1	38.4	0.3	45.8	3.8
Ce	86.6	2.7	84.0	3.1	68.6	1.3	116.9	7.0
Nd	51.4	0.7	29.4	0.3	18.4	0.5	61.1	3.3
Sm	9.48	0.34	3.86	0.08	2.37	0.09	10.50	0.59
Eu	2.61	0.10	1.07	0.02	0.73	0.03	3.03	0.11
Gd	6.69	0.40	3.05	0.08	2.05	0.03	6.96	0.27
Dy	4.10	0.20	2.49	0.10	2.37	0.05	4.22	0.18
Ho	0.71	0.04	0.50	0.02	0.52	0.01	0.71	0.04
Er	1.80	0.06	1.40	0.01	1.54	0.05	1.81	0.08
Yb	1.34	0.05	1.21	0.01	1.45	0.12	1.45	0.05
Lu	0.19	0.01	0.17	0.01	0.21	0.00	0.21	0.01
Hf	0.87	0.11	0.33	0.02	0.26	0.06	0.33	0.01
Ta	3.57	0.61	5.96	0.48	5.14	0.17	4.62	0.15
Pb	1.33	0.09	2.37	0.03	5.12	0.36	2.21	0.10
Th	1.05	0.10	1.13	0.28	4.75	0.19	3.07	0.27
U	0.24	0.02	0.13	0.01	0.94	0.02	0.65	0.01

sure-sensitive equilibria such as that based on partitioning of Ca between olivine and cpx (Köhler and Brey, 1990) are also temperature dependent, with the result that attempting to calculate temperatures and pressures simultaneously tends to produce results smeared out along a P–T path (which resembles an artificial, and unrealistic, geotherm). For the sake of transparency, we have therefore assumed a pressure of 1.5 GPa for all samples. Fortunately, pyroxene geothermometers are relatively insensitive to pressure,
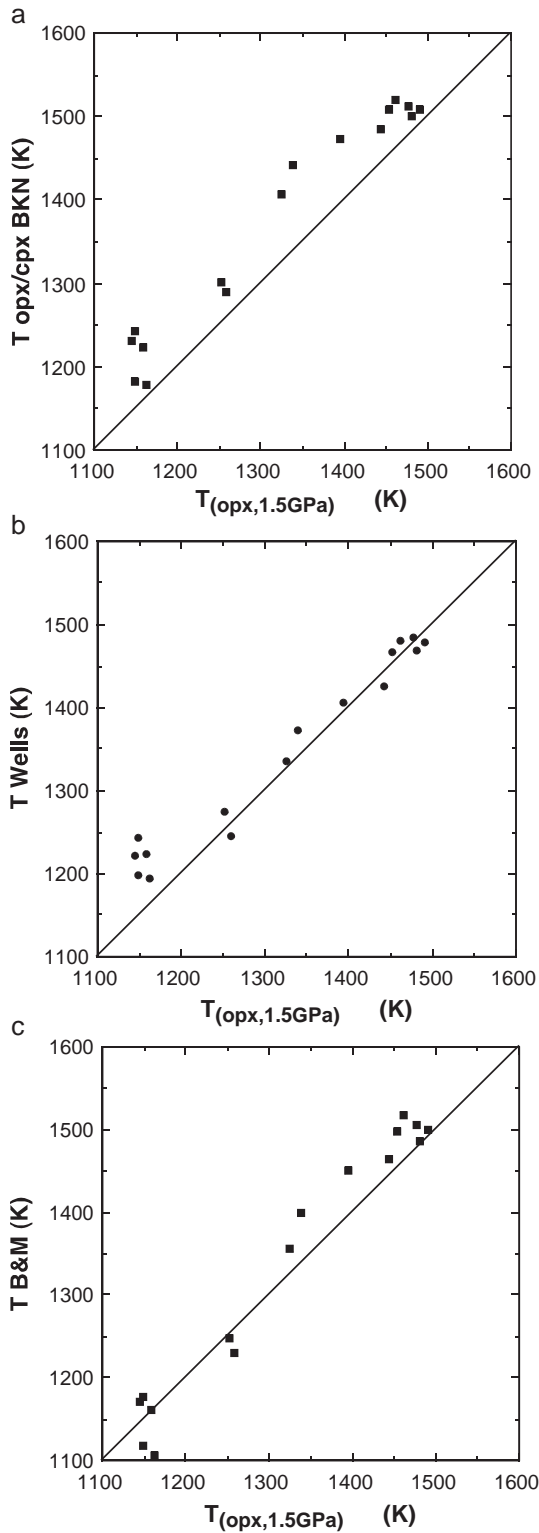
and changing the assumed pressure by ± 0.5 GPa typically changes $T_{(opx)}$ and $T_{(cpx/opx)}$ by ± 25 and 10 K, respectively. Calculated temperatures from both geothermometers are given in Table 2, and compared in Fig. 2a; comparison with a couple of earlier widely used two-pyroxene geothermometers, those of Wells (1977) and Bertrand and Mercier (1985) is made in Fig. 2b and c. Agreement is good, hence the choice of geothermometer does not influence our conclusions, although in detail Eq. (2) gives temperatures at 1.5 GPa that are systematically slightly higher than Eq. (1) (by an average of 54 K with a standard deviation of 28 K). There is no obvious correlation between the differences in calculated temperature and the chemistry of the samples, beyond the obvious effects of the Ca and Mg contents of the pyroxenes that form the basis of all pyroxene geothermometry. In the rest of this paper we shall use Eq. (1) at the assumed pressure of 1.5 GPa (labelled $T_{(opx/1.5\ GPa)}$ in the figures), which is a somewhat arbitrary decision, influenced by the relative simplicity of its formulation as well as the smoothness of some results.

Based on their calculated equilibration temperatures, we divide the 16 xenoliths into four groups:

I High temperature $(1400\ \mathrm{K} < T_{(opx/1.5\ GPa)} < 1500\ \mathrm{K})$

II Intermediate temperature 1 $(1300\ \mathrm{K} < T_{(opx/1.5\ GPa)} < 1400\ \mathrm{K})$

III Intermediate temperature 2 $(1200\ \mathrm{K} < T_{(opx/1.5\ GPa)} < 1300\ \mathrm{K})$

IV Low temperature $(1100\ \mathrm{K} < T_{(opx/1.5\ GPa)} < 1200\ \mathrm{K})$

Groups I and II are anhydrous coarse-grained to recrystallized lherzolite and harzburgite xenoliths. Group I consists of six samples, with cpx REE patterns that in one case are near to that expected for unmetasomatised mantle after melt extraction (MM1260), but otherwise are either convex-upward with maxima at Nd and Sm (MM1240, DW1342, DWv2) or LREE-enriched (DW1283, MM1213) indicating a modest

Fig. 2. Equilibration temperatures calculated from various two-pyroxene geothermometers, all at an assumed pressure of 1.5 GPa, compared against the orthopyroxene-only geothermometer of Brey and Köhler (1990), Eq. (1) in the text, which is referred to as $T_{(opx,\ 1.5\ GPa)}$; a) the clinopyroxene–orthopyroxene geothermometer of Brey and Köhler (1990), Eq. (2) in text; b) Wells (1997); c) Bertrand and Mercier (1985).

amount of metasomatism. Group II is similar but more fertile; the xenolith Mo22 is notable as it has near primitive X_{Mg}^{ol} (0.896 vs. 0.890 for the primitive mantle, O'Neill and Palme, 1998), and low $Cr_\#^{sp}$ (0.11).

Groups III and IV comprise two and five xenoliths, respectively, with tabular or mosaic equigranular textures originating by extensive shearing and recrystallization. They are considered to be equilibrated immediately below the Moho (Witt-Eickschen et al., 2003), which presently lies at a depth of about 28 km below the Eifel (Mechie et al., 1983; Raikes and Bonjer, 1983). The xenoliths bear Ti-poor pargasitic amphibole (or its breakdown products) in textural and chemical equilibrium with the coexisting minerals (Witt and Seck, 1987; Witt-Eickschen and Harte, 1994). The presence of amphibole, together with the strong enrichment of LREE over HREE, has been attributed to a pre-Quaternary metasomatic episode that affected local parts of the subcontinental lithosphere beneath the Eifel (Witt-Eickschen et al., 2003). The two group III samples (MM110 and MM766) are thought to have undergone a reheating event from about 1150–1250 K, probably caused by a thermal metamorphism from the intrusion of a magma body at the crust–mantle boundary (Witt-Eickschen et al., 1993). The pyroxenes of these reheated xenoliths are chemically zoned with Al and Cr increasing from core to rim, whereas Ca is remarkably constant (Witt-Eickschen et al., 1993).

4. Factors influencing subsolidus partitioning of trace elements in four-phase lherzolites

The trace-element partition coefficient between two phases depends on temperature, pressure, and the major-element compositions of both phases—see O'Neill and Eggins (2002) for a recent discussion. The major-element compositional effects are likely to be particularly important for those trace elements that substitute for a major element with a different ionic charge (heterovalent substitution), since charge balance requires either that the substitution is coupled with another substitution, or that cation or anion vacancies occur. Most of the incompatible trace elements commonly studied by geochemists are of this heterovalent type—e.g., the REEs, HFSEs, U and Th. For example, it is likely that the trivalent REEs substitute

into clinopyroxene (in which the major component is diopside, $CaMgSi_2O_6$) by replacing divalent Ca^{2+} in the M2 octahedral site, with charge balance maintained by Al^{3+} replacing Si^{4+} in the tetrahedral site (i.e., as $REEMgAlSiO_6$). This means that the chemical potential of the REE_2O_3 component in cpx depends on the chemical potentials of both Al_2O_3 and SiO_2.

However, four-phase lherzolites have a low thermodynamic variance (few degrees of freedom), such that the chemical potentials of their major-element components are almost independent of composition, being accordingly specified mainly by temperature and pressure. As pressure is generally highly correlated with temperature in the Earth's interior, there is, to a first approximation, just one important independent variable (or degree of freedom) in our suite of xenoliths, namely temperature. This is the first-order approximation; the departures from this approximation will now be discussed.

More than 98% of a typical lherzolite consists of just the five major-element components SiO_2, MgO, FeO, CaO and Al_2O_3 (e.g., O'Neill and Palme, 1998); with five components and four phases, the compositions of all phases are completely fixed by specifying temperature, pressure and just one compositional variable, such as (conveniently) X_{Mg}^{ol} (molar Mg/($Mg+Fe$) of olivine). The total variation of X_{Mg}^{ol} in typical spinel-lherzolite xenoliths is from 0.89 (primitive mantle) to ~0.92 (cpx out), which may be significant petrologically but is trivial in thermodynamic terms, and can be ignored. The xenoliths used in this study actually span an even lower range of X_{Mg}^{ol}, all but two being within the range 0.913–0.921 (Table 2).

The only temperature-independent variations in the compositions of the phases in a four-phase lherzolite are therefore due to the minor components, which make up less than 2% of the mantle composition. In the present context, the most influential of these components is Cr_2O_3, because Cr^{3+} substitutes for octahedrally coordinated Al in pyroxenes and spinel (or garnet), lowering the activity of Al_2O_3 in the system (e.g., Liu and O'Neill, 2004). This effect reduces Al_2O_3 in pyroxenes considerably, and is particularly important in the spinel-lherzolite facies (Klemme and O'Neill, 2000; Liu and O'Neill, 2004). Alumina in pyroxenes is needed to charge-balance many heterovalent substitutions, as pointed out above for the REE. In the spinel-lherzolite assemblage, the chemical po-

tential of Cr_2O_3 can be characterized by the Cr# of the spinel (molar $Cr/(Al+Cr)$). Our xenoliths cover a useful range, from Cr#=0.11 to 0.47. However, since the Cr_2O_3 substitution affects Al_2O_3 in cpx and opx in the same way, its influence should mostly cancel out in cpx/opx partition coefficients.

The next most influential minor component is Na_2O, which is heavily concentrated into cpx. Unlike Cr_2O_3, therefore, this component can be expected potentially to affect cpx/opx partition coefficients. The Na_2O contents of the cpx in our xenoliths are quite low, but still vary by a factor of two (Table 2), which, we shall show, is sufficient to influence many partition coefficients. Deducing this is only possible because Na_2O is not correlated with temperature in our samples (Table 2). Although an inverse correlation between Na_2O and Cr# might be expected on the grounds that the former decreases while the latter increases with melt extraction, no such correlation is observable in our samples, presumably because of subsequent metasomatism. For our present purposes this is convenient as it allows us to treat these two variables as independent in our statistical examination of the partitioning data. However, TiO_2 generally does correlate with Na_2O (being, like Na_2O, moderately incompatible), such that crystal-chemical effects of Ti would not be statistically resolvable; in any case, the lower abundance of TiO_2 and its more even distribution between cpx and opx means that it is unlikely to have much influence on trace-element partitioning in our samples.

Remaining potential minor variables include redox state and water content. Calculated values of $\Delta\log fO_2$ relative to QFM (Table 2) show that the lower temperature xenoliths (Groups III and IV) are more oxidized relatively, which is consistent with their more metasomatised nature (cf. McCammon et al., 2001) and is correlated with the presence of amphibole (or its breakdown products). While redox state could be important in controlling the partitioning of polyvalent elements, the variation in redox states in our samples is probably too small to be significant, at least for any trace elements considered in this study. In any case, since the inferred variation of redox state correlates empirically with temperature in our sample suite, it is unlikely that we would be able to disentangle the effects from those of temperature.

The primary water content of the minerals in the xenoliths is unknown; however, the seven lowest temperature xenoliths contained pargasitic amphibole as an extra phase (Table 2). The nominally anhydrous minerals in these samples would therefore have relatively high H_2O contents, the level of H_2O being defined by amphibole saturation at the P–T conditions of equilibration, e.g., according to the reaction:

$$2 \underset{cpx}{CaMgSi_2O_6} + 2.5 \underset{opx}{Mg_2Si_2O_6} + H_2O$$

$$= \underset{amphibole}{Ca_2Mg_5Si_8O_{22}(OH)_2} + \underset{ol}{Mg_2SiO_4} \qquad (3)$$
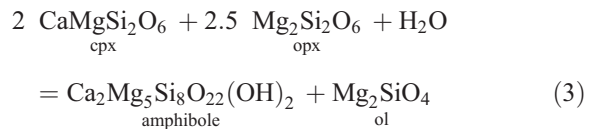
The presence of H_2O may potentially be an important control on heterovalent incompatible-element substitutions in some phases, although little is known about this at present.

In summary: we expect that almost the entire variation of inter-crystalline trace-element partition coefficients in our 16 samples will depend on just one independent variable, temperature. This variation will include not only the direct effect that temperature has on the thermodynamics of the partitioning reaction, but also indirect effects that arise through the covariation of temperature with both pressure and mineral compositions in four-phase spinel lherzolites; this always needs to be kept in mind when attempting to make deductions about the controls on partitioning behaviour from the empirical correlations of partition coefficients with temperature. In addition, minor contributions from the molar $Cr(Cr+Al)$ ratio in spinel (Cr#^{sp}), Na in cpx (N_{Na}^{cpx}, the number of Na cations per formula unit of 6 oxygens), and possible differences between anhydrous and hydrous samples will be looked for.

4.1. Data fitting and extrapolation

Since the main reason for undertaking this study is to extrapolate partition coefficients to the temperatures appropriate for mantle melting, to see how trace elements are distributed among the solid phases during melting, the reliability of such extrapolations needs some comment. The Nernst partition coefficient $D_M^{\alpha/\beta}$ (defined as the concentration of M in phase α divided by the concentration of M in phase β) is not a rigorous thermodynamic entity.

The reason is that M (or its simple oxide) is in general not a thermodynamically valid component in the context of a partitioning reaction, as it cannot be varied independently (see, for example, a recent discussion in O'Neill and Eggins, 2002). For the thermodynamics of element partitioning to be described rigorously it is necessary to use the equilibrium constant, K_M, which is defined for an appropriately balanced partitioning reaction, and includes the activities of those major-element components involved in the substitution of M into both phases (the "stoichiometric controls"). However, as discussed above, the activities of major-element components (SiO_2, CaO, MgO and FeO) are more-or-less buffered in a four-phase lherzolite. The exception is the activity of Al_2O_3 due to variable Al/Cr ratios. This buffering of the major-element components involved in the "stoichiometric control" allows empirical values of $D_M^{\alpha/\beta}$ to be related to a suitable equilibrium constant K_M straightforwardly.

For high-temperature partitioning reactions, the simplified relationship $\ln K_M = -\Delta_r H^\circ / RT + \Delta_r S^\circ / R$ is generally an excellent approximation at constant pressure, as $\Delta_r Cp^\circ$ is usually small. Hence the algebraic form of the relationship between $D_M^{\alpha/\beta}$ and temperature should be simply be $\ln D_M^{\alpha/\beta} \propto 1/T$. In the context of the present study, this relationship should hold best for cpx/opx partitioning, since the "stoichiometric controls" on trace-element substitution are likely to be the same in both pyroxene phases due to their similar stoichiometry, and, as regards the unbuffered major element component Al_2O_3, their similar Cr/Al ratios.

In light of these considerations, we have fitted our empirical values of $D_M^{\alpha/\beta}$ (i.e., $D_M^{cpx/opx}$ etc.) to the general equation:

$$\ln D_M^{\alpha/\beta} = a_0 + \left(a_1 + a_2 \cdot N_{Na}^{cpx} + a_3 \cdot Cr\#^{sp}\right) T_{(opx,\ 1.5GPa)} \tag{4}$$

The fitting was carried out by multiple non-linear least-squares regression with uncertainties in $D_M^{\alpha/\beta}$ as calculated from Table 3, or $\pm 5\%$, one standard deviation, whichever is the larger, and in $T_{(opx,\ 1.5GPa)}$ of ± 10 K. Obviously $T_{(opx,\ 1.5GPa)}$ must be the same for every element in each sample and should not be treated as independently variable in the different regressions, but we have ignored this complication

for the sake of computational simplicity. This could be rationalised as allowing for some imperfection in equilibration for trace elements. We ignored the uncertainties in N_{Na}^{cpx} and $Cr\#^{sp}$, which have an insignificant effect.

For pairs of elements with similar geochemical properties (i.e., same valence and fairly similar ionic radii, such as the REEs), the two-element distribution coefficient, which is given by the ratio of the partition coefficients $KD_{M/N}^{\alpha/\beta} = D_M^{\alpha/\beta} / D_N^{\alpha/\beta}$, should approximate a true equilibrium constant, because the "stoichiometric control" on each element in each phase cancels out across the exchange reaction (e.g., O'Neill and Eggins, 2002). Furthermore, the entropies of such exchange reactions are expected to be small, hence the simple relationship $\ln KD_{M/N}^{\alpha/\beta} \approx -\Delta_r H^\circ / RT$, with $KD_{M/N}^{\alpha/\beta}$ tending to unity as T goes to infinity.

5. Results and discussion

5.1. Rare Earth Elements (REE) and Y

The REE and Y are concentrated into cpx, but with significant amounts also in opx. Only Y and the four heaviest REE analysed in this study, namely Ho, Er, Yb and Lu, are above detection limits in olivine in the majority of the samples. In spinel, only Y, at 5–15 ppb in most samples, is above the limit of detection (~2 ppb); hence, because of its low modal abundance in peridotites, spinel holds a negligible proportion of the REEs.

Fig. 3 shows $\ln D_{REE}^{cpx/opx}$ vs. $1/T_{(opx,\ 1.5GPa)}$. The values of $D_{REE}^{cpx/opx}$ decrease systematically with increasing atomic number; there is a large temperature effect for all the REE, but this effect also deceases with increasing atomic number. If we extrapolate these partition coefficients to the dry solidus, values of $D_{REE}^{cpx/opx}$ would only be about 2–3 for the heavy REE. This is in agreement with experimental measurements (e.g., Salters et al., 2002; McDade et al., 2003). Since the modal abundance of opx is initially about twice that of cpx for fertile mantle at its solidus in the spinel-lherzolite facies, and the ratio of opx to cpx increases with melt extraction, it is apparent that the major proportion of the heavy REEs in the residues of anhydrous partial melting
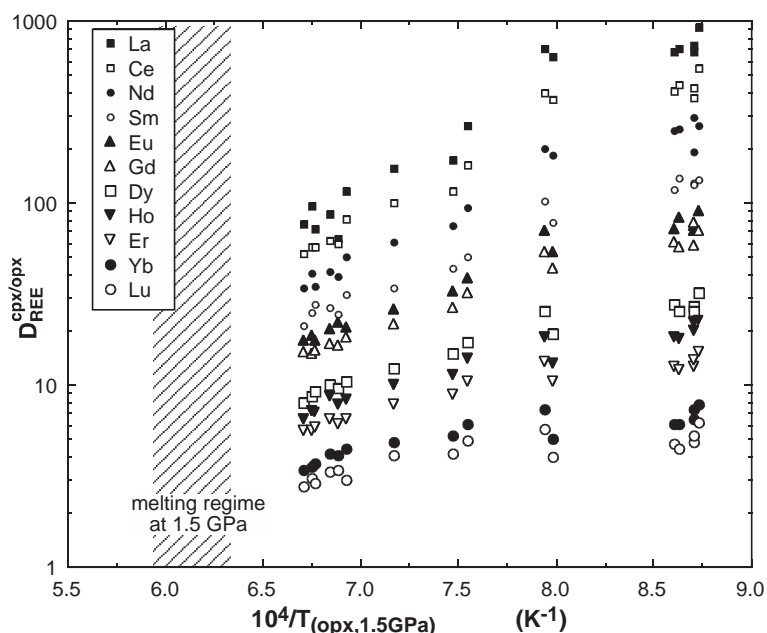
Fig. 3. Partitioning of REEs between cpx and opx as a function of temperature ($T_{(opx, 1.5 GPa)}$). The region from the anhydrous peridotite solidus at 1.5 GPa (1308 °C according to Hirschmann, 2000) to an estimated cpx-out temperature at 1420 °C is shown shaded and labeled as the "melting regime". Note that much of the apparent scatter in the data as plotted is due to the effect of Na in cpx, which has not been accounted for in this two-dimensional representation.

are actually held in opx. Even for the light REE, the values of $D_{REE}^{cpx/opx}$ become less than 30 over the melting interval at 1.5 GPa (Fig. 3). For refractory residues with only a few percent residual cpx, such as typical abyssal peridotites, much of the light REE inventory will also reside in opx.

To test whether some of the scatter in the trends in Fig. 3 may be due to compositional effects we fitted the data for each REE and Y to Eq. (4). For all REE and Y, the last term (in $Cr\#^{sp}$) was found to be insignificant and was dropped, but the terms in N_{Na}^{cpx} proved to be significant. Results from the regression analysis for $a0$, $a1$, and $a2$ for each REE and Y are given in Table 4 and are plotted as a function of ionic radius in 8-fold coordination (from Shannon, 1976) in Fig. 4. The parameters $a0$ and $a1$ show a linear dependence, that of $a2$ approximately parabolic. These good systematic relationships prompted us to refit the data globally to a single equation:

$$\ln D_{REE}^{cpx/opx} = a_0 + b_0 R_{REE}^{VIII} + (a_1 + b_1 R_{REE}^{VIII})/T_{(opx,\ 1.5GPa)}$$
$$+ \left(a_2 + b_2 R_{REE}^{VIII} + c_2 \left(R_{REE}^{VIII}\right)^2\right) N_{Na}^{cpx} \qquad (5)$$

The resulting best-fit parameters are:

$$a_0 = 18.11,\ b_0 = -0.192 pm^{-1}$$

$$a_1 = -50568 K^{-1},\ b_1 = 542 K^{-1} pm^{-1}$$

$$a_2 = -560755,\ b_2 = 10644 pm^{-1},\ c_2$$
$$= -49.8 pm^{-2}$$

The values of R_{REE}^{VIII} from Shannon (1976) are (in pm): La 116.0; Ce 114.3; Pr 112.6; Nd 110.9; Sm 107.9; Eu 106.6; Gd 105.3; Tb 104.0; Dy 102.7; Ho 101.5; Er 100.4; Tm 99.4; Yb 98.5; Lu 97.7; and Y 101.9. There is no hint of an Eu anomaly in these $D_{REE}^{cpx/opx}$ data.

An interesting detail of the thermodynamics of REE incorporation in pyroxenes is revealed by the two-element distribution coefficients $KD_{REE/Y}^{cpx/opx}$, corresponding to the exchange reactions: $[REE]_{opx} + [Y]_{cpx} = [REE]_{cpxs} + [Y]_{opx}$. Note that $KD_{REE/Y}^{cpx/opx} = D_{REE}^{cpx/opx}/D_Y^{cpx/opx}$, so nothing new is being introduced here; but the two-element distribution coefficient eliminates the stoichiometric control, much of the effect of activity coefficients, and the need to

Table 4
Partitioning of incompatible trace elements between clinopyroxene and orthopyroxene: fits of data in Table 3 by multiple non-linear regression to the semi-empirical equation: $\ln D_M^{cpx/opx} = a_0 + (a_1 + a_2 N_{Na}^{cpx} + a_3 Cr\#^{sp})/T_{(opx, 1.5GPa)}$ where N_{Na}^{cpx} is the number of atoms of Na in cpx per formula unit of six oxygens, and $Cr\#^{sp}$ is molar $Cr/(Al+Cr)$ in coexisting spinel

Element	a_0	a_1	a_2	a_3	χ_v^2
REE and Y					
La	-3.94 ± 0.33	$11,394 \pm 418$	$13,568 \pm 2523$	–	3.10
Ce	-3.28 ± 0.24	$10,329 \pm 345$	8504 ± 1718	–	3.23
Nd	-3.32 ± 0.26	9951 ± 374	4782 ± 1991	–	1.16
Sm	-2.85 ± 0.30	8638 ± 393	3644 ± 2246	–	0.83
Eu	-2.27 ± 0.24	7495 ± 339	3006 ± 2064	–	0.66
Gd	-2.34 ± 0.22	7263 ± 279	3562 ± 1641	–	0.85
Dy	-1.66 ± 0.17	5425 ± 228	4485 ± 1198	–	0.63
Ho	-1.56 ± 0.17	4907 ± 250	5166 ± 1178	–	0.95
Er	-1.05 ± 0.17	3856 ± 224	5158 ± 1113	–	0.61
Yb	-0.61 ± 0.15	2496 ± 200	6070 ± 980	–	1.14
Lu	-0.71 ± 0.16	2254 ± 198	6578 ± 1066	–	1.63
Y	-1.26 ± 0.15	4402 ± 209	5290 ± 1052	–	0.45
HFSE					
Ti	-1.09 ± 0.14	2145 ± 200	8552 ± 973	–	2.32
Zr	-4.09 ± 0.20	7381 ± 279	$10,360 \pm 1373$	1026 ± 285	0.69
Hf	-3.61 ± 0.37	6868 ± 458	$10,500 \pm 2285$	870 ± 420	0.46
Nb	-5.16 ± 0.25	7822 ± 371	$21,414 \pm 1838$	–	4.23
Ta	-5.62 ± 0.70	$10,176 \pm 850$	$19,131 \pm 5266$	–	0.48
Th[a]	-2.21 ± 0.76	6876 ± 802	$18,917 \pm 3681$	–	4.17
U[b]	-3.36 ± 0.85	7465 ± 1075	$14,141 \pm 4050$	–	1.69
Others					
Sc[c]	-2.35 ± 0.15	4207 ± 198	3500	–	0.67
Sr[d]	-4.02 ± 0.28	$12,405 \pm 391$	–	–	1.73
"	-4.23 ± 0.31	$11,992 \pm 443$	4183 ± 1781	1146 ± 349	0.71
Ba[e]	-3.39 ± 0.90	7449 ± 1185	$11,800 \pm 6521$	3478 ± 1304	1.57
Pb[f]	-7.66 ± 0.73	$10,555 \pm 923$	$17,169 \pm 6431$		2.40

Data were weighted assuming uncertainties (1σ) in $D_M^{cpx/opx}$ of $\pm 5\%$ or as observed, whichever is larger, and ± 10 K in $T_{(opx, 1.5GPa)}$. Uncertainties in N_{Na}^{cpx} and $Cr\#^{sp}$ were ignored.
[a] 13 data; [b] 10 data; [c] One datum (DW 211) omitted; [d] One datum (M766) omitted; [e] Two data (MM1278 and DW1342) omitted; [f] One datum (DW1284) omitted.

convert from concentrations (ppm) to mole fractions, all of which should make the thermodynamic relationships more transparent. We chose Y as the common element as its higher cosmochemical abundance means that it is relatively accurately determined even in opx, and its properties put it in the middle of the REE spectrum (its geochemical twin is Ho). Fig. 5 shows $\ln KD_{REE/Y}^{cpx/opx}$ vs. $1/T_{(opx, 1.5GPa)}$. For such an exchange reaction it is usually expected that the entropy of reaction is zero, hence $\ln KD_{REE/Y}^{cpx/opx} = \Delta_r H^\circ / RT$, and each line should intersect at $\ln KD_{REE/Y}^{cpx/opx} = 0$ at $1/T = 0$ (i.e., $KD_{REE/Y}^{cpx/opx}$ should go to unity as T goes to infinity). Clearly this does not

happen, the common intersection being indeed at $KD_{REE/Y}^{cpx/opx} = 0$, but at $T_{(opx, 1.5GPa)} = 2720$ K (in this analysis we neglect the fact that the effect of N_{Na}^{cpx} varies among the REE, which introduces a bit more scatter in the data particularly for La and Ce, but the conclusions are robust). Two end-member explanations (not mutually exclusive) are possible:

1) $\Delta_r S^\circ$ is not zero, but correlates systematically with $\Delta_r H^\circ$
2) There is an equally systematic pressure dependence of the exchange reaction (i.e., $\Delta_r V^\circ$), which we are not accounting for, as we are not
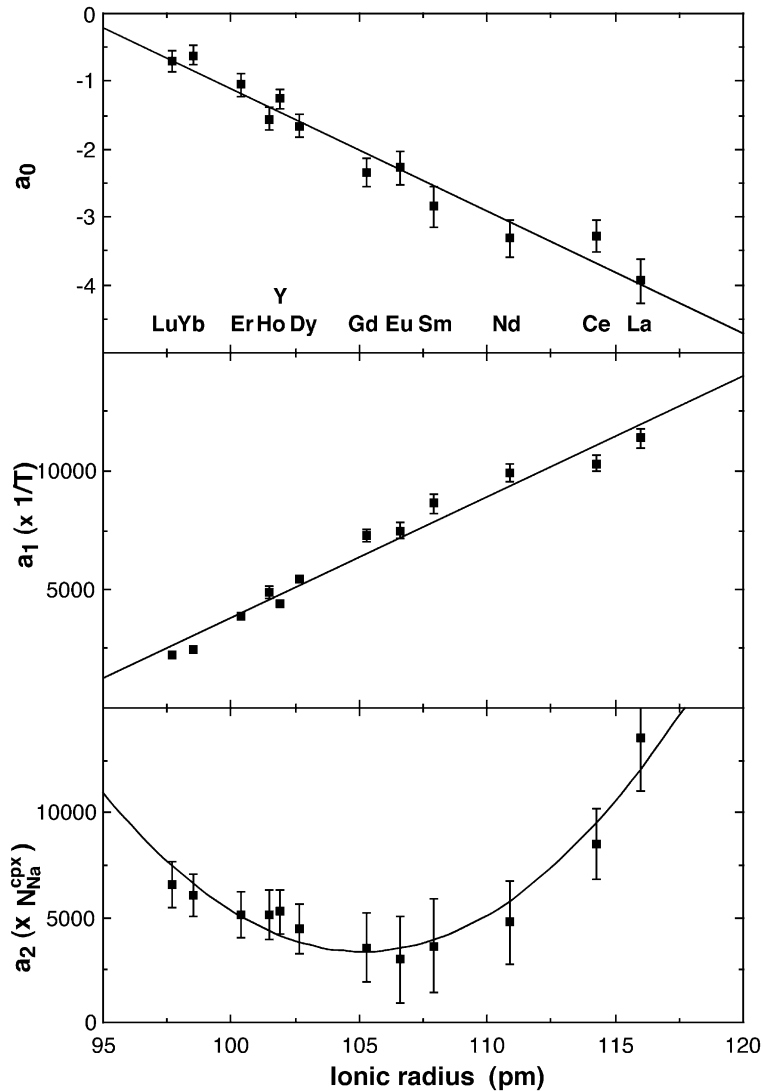
Fig. 4. REE partitioning between cpx and opx: results from least squares fitting of the equation $\ln D_{\text{REE}}^{\text{cpx/opx}} = a_0 + (a_1 + a_2 \cdot N_{\text{Na}}^{\text{cpx}} + a_3 \text{Cr#}^{\text{sp}})/T_{(\text{opx, 1.5GPa})}$, plotted as a function of the REE 3+ cation in 8-fold coordination (from Shannon, 1976). The parameters a_0 and a_1 are linear functions of the ionic radius, and a_2 is approximately parabolic.

using pressure as an independent variable. (As explained above, this is mainly because we expect pressure to correlate with temperature in mantle xenoliths, but also because we do not know the equilibration pressure of our samples accurately).

Since there is a general expectation that $\Delta_r V^{\circ}$ should correlate with $\Delta_r S^{\circ}$, some combination of

both explanations is probable. Non-zero values of $\Delta_r V^{\circ}$ may originate because there is a difference in coordination geometry of the M2 site between clinopyroxene and orthopyroxene; the site geometries are akin to distorted 8-fold coordination in the former, but distorted 6-fold coordination in the latter. The somewhat unexpected feature is how good the systematic correlation of $\Delta_r S^{\circ}$ and/or $\Delta_r V^{\circ}$ with $\Delta_r H^{\circ}$ is.
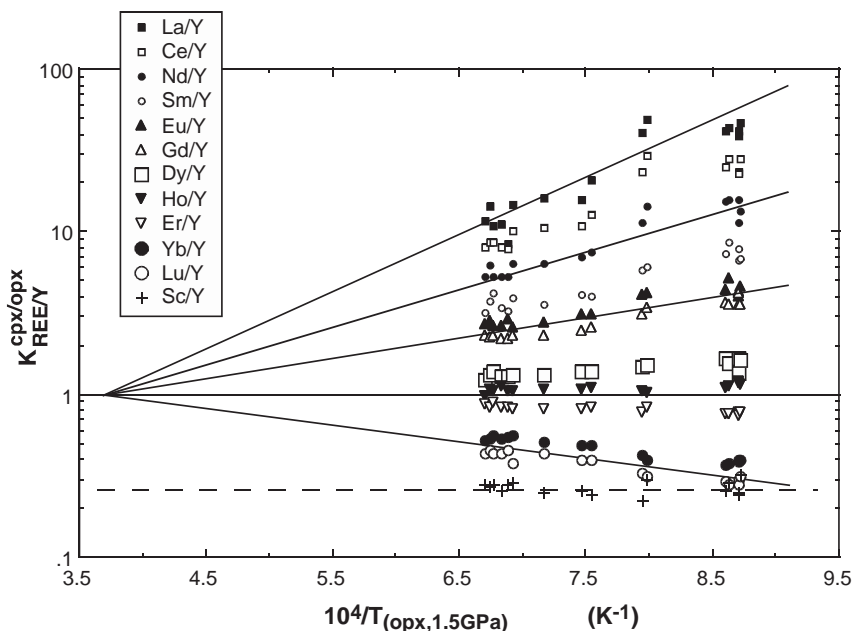
Fig. 5. The two-element distribution coefficient $KD_{REE/Y}^{cpx/opx}$, plotted as $\ln KD_{REE/Y}^{cpx/opx}$ against inverse temperature ($1/T_{(opx, 1.5G Pa)}$). The curves for all REE intersect at a common point, at 2720 K and $\ln KD_{REE/Y}^{cpx/opx} = 0$. This behaviour is not expected from simple thermochemical arguments, which would predict an intersection at infinite temperature (see text). Note that Sc does not follow the same trend, perhaps because the Sc^{3+} cation, which is considerably smaller than REE^{3+} cations, substitutes into the M1 site in pyroxenes rather than the larger M2 site.

Sorting this out highlights a need for some experimental input, since T and P can be varied independently in experiments. If the non-zero $\Delta_r V^\circ$ explanation is found to be significant, the partitioning of REE and Y between cpx and opx might make a useful geobarometer.

In Fig. 5 we have also plotted $KD_{Sc/Y}^{cpx/opx}$, which shows a quite different trend to the $KD_{REE/Y}^{cpx/opx}$ data. This is probably because Sc^{3+} substitutes into the M1 site of the pyroxene structure, and not, like the REE, into M2.

5.1.1. REE in olivine

Values of $D_{REE}^{cpx/ol}$ for Ho, Er, Yb, Lu and Y are plotted versus $1/T_{(opx, 1.5 GPa)}$ in Fig. 6, and empirical equations describing the partitioning behaviour are given in Table 5. The amounts of Ho, Er and Lu in ol are not far above detection limits in most samples, hence the scatter in the data. Nevertheless, there is a clear correlation with temperature, extrapolating to values of about 20 for $D_{Yb}^{cpx/ol}$ and $D_{Lu}^{cpx/ol}$ in the melting regime. Thus in highly depleted peridotites such as abyssal peridotites with modal ol/cpx ratios

greater than 20, the ol will actually hold more of the rock's heavy REE than the cpx. However, most of the heavy REE inventory, and a significant part of the light REEs too, will be held in opx.

5.1.2. Intercrystalline partitioning of REEs as a function of ionic radius

Values of $\ln D_{REE}^{cpx/opx}$ and $\ln D_{REE}^{cpx/ol}$ for Mo22 determined both in this study and by Stosch (1982) are plotted against ionic radius (R_{REE}^{VIII}) in Fig. 7. All sixteen of our samples show similarly monotonically increasing, smooth patterns of $\ln D_{REE}^{cpx/opx}$ vs. R_{REE}^{VIII}, whereas several of the other spinel lherzolites analysed by Stosch (1982) show minima in this pattern somewhere between Ce and Sm, e.g., the samples Ib/3, Ib/8, KH-K8 and SC-K2 in his Fig. 5. Unless REE partitioning in these samples is controlled by some unknown crystal-chemical feature not present in our samples, it is likely that such an effect is due to chemical disequilibrium. The rate of diffusion of the REE in cpx decreases systematically with increasing ionic radius (van Orman et al., 2001), i.e., La is more sluggish than Lu; hence on cooling from high temper-
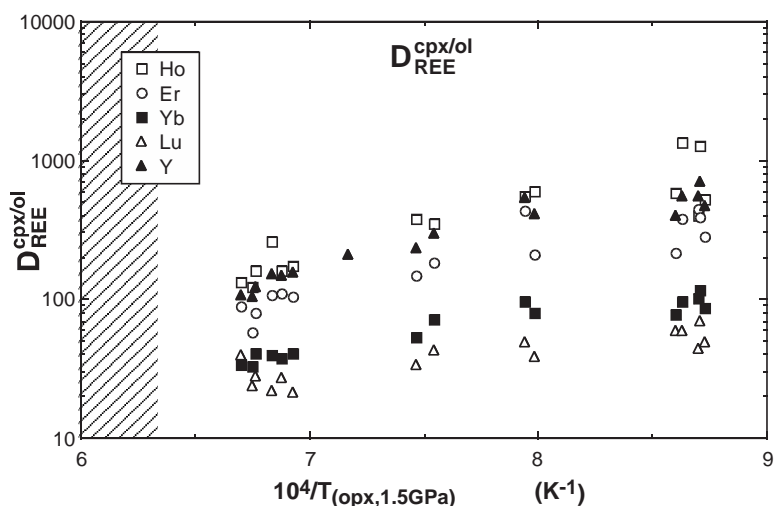
Fig. 6. Partitioning of heavy REEs and Y between cpx and ol. The REEs lighter than Ho are generally below our limit of detection in ol. Extrapolation of the partitioning trends to magmatic temperatures (shaded region) shows that ol will contain a significant proportion of the heaviest REEs in depleted peridotites.

ature, values of $D_{REE}^{cpx/opx}$ for the light REE will tend to increase less rapidly than for the heavy REE. This raises the question of whether the even more marked deviations from a monotonic curve of ln $D_{REE}^{cpx/ol}$ vs. IR shown by all eight of the samples analysed by Stosch (1982), including Mo22 (kinked at Nd, see his Fig. 6), is also a disequilibrium feature, or perhaps an analytical artefact caused by the very low levels of light REE in olivine. We are not aware of any crystal-chemical reason why the partitioning of

REEs into olivine should not decrease monotonically from Lu to La. This is potentially an important point in determining the significance of REE patterns in very depleted olivine-rich rocks such as melt-channel dunites, or in melt inclusions trapped in olivine. Unfortunately, our results cannot test this, as the light REEs are below the detection limit of LA-ICP-MS in all our xenoliths.

5.2. Scandium

The partitioning of Sc between cpx, opx and ol follows very well defined trends as a function of temperature (Fig. 8), although Sc in opx in one sample (DW 211) seems to be anomalously low. Apart from this, most of the scatter of the data in this diagram is due to the effect of Na in cpx. Regression of the data gives:

$$\ln D_{Sc}^{cpx/opx} = -2.354 + \left(4207 + 3500 N_{Na}^{cpx}\right)/T$$
$$\left(\chi_v^2 = 0.67\right)$$

$$\ln D_{Sc}^{cpx/ol} = -1.696 + \left(5481 + 3500 N_{Na}^{cpx}\right)/T$$
$$\left(\chi_v^2 = 2.56\right)$$

$$\ln D_{Sc}^{opx/ol} = 0.485 + 1511/T \qquad \left(\chi_v^2 = 0.89\right)$$

Table 5
Partitioning of incompatible trace elements between clinopyroxene and olivine: fits of data in Table 3 by multiple non-linear regression to the semi-empirical equation: ln $D_M^{cpx/ol} = b_0 + (b_1 + a_2 N_{Na}^{cpx} + a_3 Cr\#^{sp})/T_{(opx, 1.5GPa)}$ where the parameter a_2 is constrained from the cpx/opx data–see Table 4 for further details

Element	a_0	a_1	a_2	χ_v^2
REE and Y				
Ho	2.64 ± 0.56	3727 ± 714	5200	1.93
Er	1.22 ± 0.43	7786 ± 594	5200	2.00
Yb	0.05 ± 0.24	4866 ± 317	6100	1.41
Lu	0.19 ± 0.54	3925 ± 691	6600	0.62
Y	-0.22	7199 ± 310	5300	2.97
Others				
Sc	-1.70 ± 0.15	5480 ± 196	3500	2.56
Sr[a]	1.70 ± 1.06	$10,494 \pm 1524$	–	1.03

[a] One datum (MM1260) omitted.
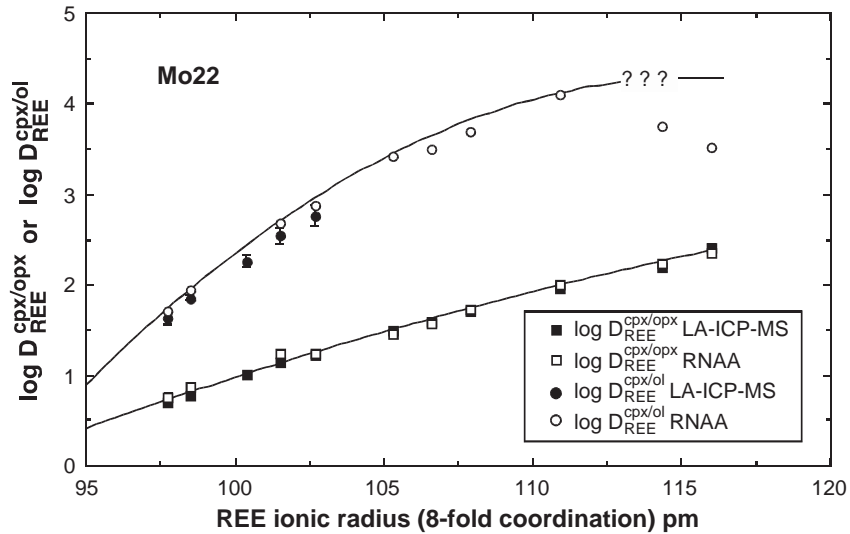
Fig. 7. Comparison of values of $D_{REE}^{cpx/opx}$ and $D_{REE}^{cpx/ol}$ plotted against ionic radius (R_{REE}^{VIII}) from this study and from Stosch (1982). The latter was able to determine the light REE in olivine, which are below the limits of detection in this study (c. 1 ppb). However, the values of Ce and La in ol reported by Stosch fall off the extrapolation of the curve of ln $D_{REE}^{cpx/ol}$ vs. R_{REE}^{VIII}, which may indicate that these values are compromised by contamination.

For $D_{Sc}^{cpx/opx}$ and $D_{Sc}^{cpx/ol}$, the coefficients in N_{Na}^{cpx} were constrained to be the same. The partitioning of Sc between cpx and opx in peridotitic and websteritic upper-mantle xenoliths has previously been investigated by Seitz et al. (1999), using SIMS. Their results are compared in Fig. 9a. There is good agreement for the peridotitic samples, but the websterites plot systemat-

ically at higher values of $D_{Sc}^{cpx/opx}$. In Fig. 9b we show that this is caused by a dependence of $D_{Sc}^{cpx/opx}$ on the Mg# of the pyroxenes, by plotting the difference between calculated and measured values of $D_{Sc}^{cpx/opx}$ versus the Mg# of the opx. An effect of Fe on Sc partitioning was previously postulated by Glassley and Piper (1978). Since all our samples are all at
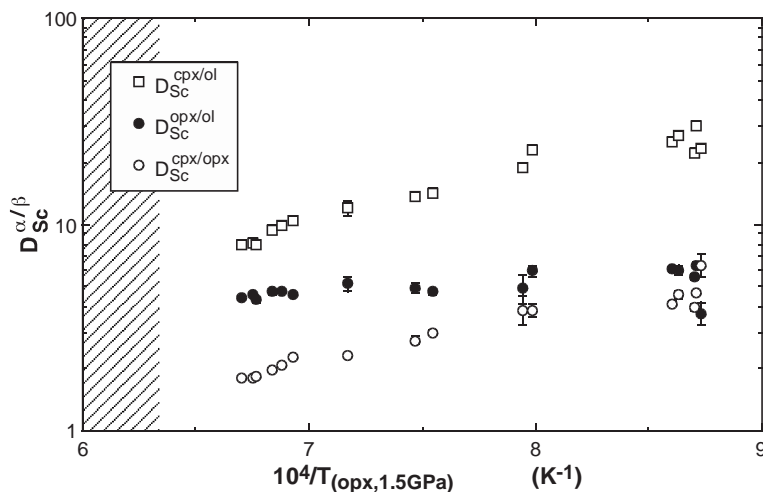
Fig. 8. Partitioning of Sc between cpx, opx and ol as a function of $T_{(opx, 1.5\ GPa)}$. Error bars (one s.d.) are shown where they are larger than the symbol. Much of the scatter is accounted for by the effect of Na in cpx (N_{Na}^{cpx}).

essentially the same Mg# (Table 2) we cannot expect to pick up any effect of Mg# from our data. The example of Sc should therefore provide a warning that our empirical partitioning relationships should not be extrapolated to different compositions with different Mg#s, for any element.

Spinel also contains detectable Sc (Table 3d). The partitioning of Sc between cpx and sp can be empirically described by:

$$\ln D_{Sc}^{cpx/sp} = -1.804 + (7901 - 4298 Cr\#^{sp} + 3500 N_{Na}^{cpx})/T \qquad (\chi_v^2 = 4.2) \qquad (6)$$

Despite invoking the extra term in Cr#^{sp}, the fit is markedly less good than for the partitioning among
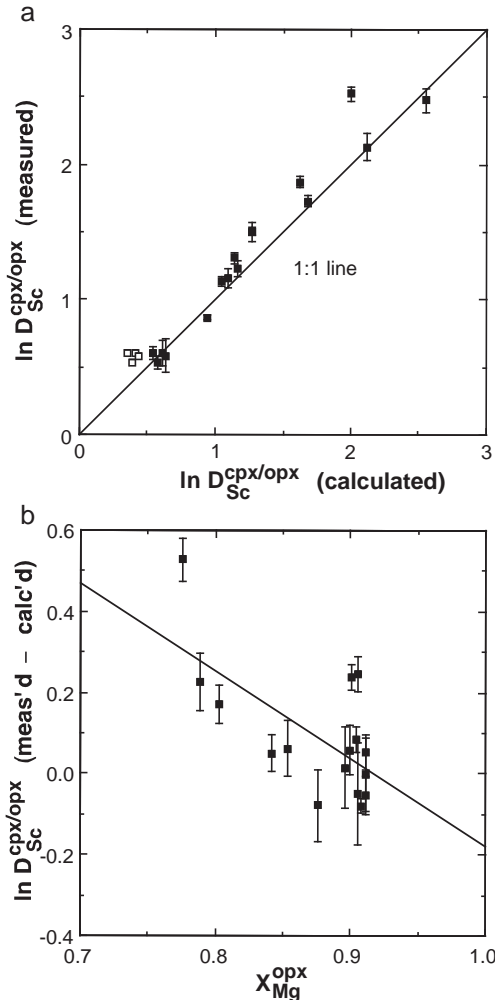
pyroxenes and olivine. The sign of the term in Cr#^{sp} is such that Sc correlates with Cr in spinel, as might be expected from the smaller difference in the ionic radii between Sc and Cr^{3+} than between Sc and Al. This manifests itself in an empirical correlation between the Sc content of the spinel and Cr#^{sp} in our 16 samples.

5.3. High field strength elements (Ti, Zr and Hf, Nb and Ta, plus U and Th)

The correlations of $D_{Hf}^{cpx/opx}$ with $D_{Zr}^{cpx/opx}$ and of $D_{Ta}^{cpx/opx}$ with $D_{Nb}^{cpx/opx}$ are shown in Fig. 10a and b. Inter alia, such systematic relationships test the quality of the data, e.g., the good correlation of Nb with Ta implies that the potential isobaric interference of $^{53}Cr + ^{40}Ar$ on ^{93}Nb is not important in pyroxenes. Fig. 11a shows the relationships of $\ln D_{HFSE}^{cpx/opx}$ versus $1/T_{(opx, 1.5 \ GPa)}$. As with the REEs, the HFSEs partition into cpx, but the values of $D_{HFSE}^{cpx/opx}$ are sensitive to temperature, and in particular the amounts of Zr and Hf held in opx become significant at solidus temperatures. The data confirm the experimental observation of Wood et al. (1999) that U is somewhat less incompatible than Th in opx compared to cpx (i.e., $D_U^{cpx/opx} < D_{Th}^{cpx/opx}$, as shown in Fig. 11b). This could potentially be of importance in interpreting U decay series data. The fits to Eq. (5) for all HFSEs plus U and Th are included in Table 4.

Fig. 9. a) Partitioning of Sc between cpx and opx: the results of Seitz et al. (1999) using SIMS compared with the equation derived from the present work, using $T_{(opx, 1.5 \ GPa)}$. Samples include both garnet and spinel lherzolites and garnet websterites. Values of $D_{Sc}^{cpx/opx}$ were calculated using T_{opx} (method of Brey and Köhler, 1990) at an assumed single pressure of 1.5 GPa from the major-element opx and cpx analyses of Seitz et al.; these are shown as solid symbols with error bars (1 s.d., of the SIMS Sc analyses, as reported by Seitz et al., 1999). For the spinel lherzolites and garnet websterites, our assumed pressure of 1.5 GPa is mostly quite close to the pressures of equilibration estimated by Seitz et al., see their Table 1. For the four garnet lherzolites, which equilibrated at substantially higher pressures than the assumed 1.5 GPa, we have additionally plotted values of $D_{Sc}^{cpx/opx}$ calculated using T_{opx} at 3.3 GPa (pressure of equilibration as estimated by Seitz et al.), as open symbols. This displaces these data off the 1 : 1 line, indicating that the pressure-dependence of $D_{Sc}^{cpx/opx}$ is close to that of T_{opx}. Agreement is good for most samples, with the difference between observed and calculated values being mostly due to the lower Mg# of some of the websteritic samples in the Seitz et al. (1999) study, which is demonstrated in Fig. 9b by plotting the difference between calculated and observed values of $D_{Sc}^{cpx/opx}$ versus the Mg# of the opx.
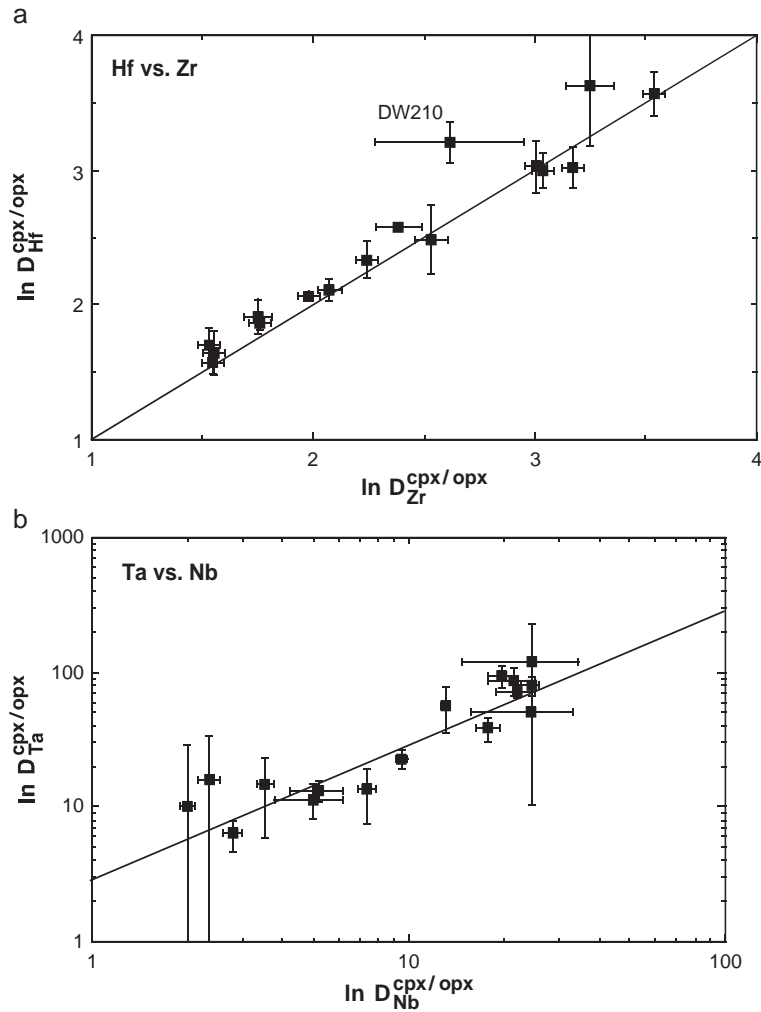
Fig. 10. "Geochemical twins" among the High Field Strength Elements (HFSEs): correlations of a) $D_{Hf}^{cpx/opx}$ with $D_{Zr}^{cpx/opx}$; b) $D_{Ta}^{cpx/opx}$ with $D_{Nb}^{cpx/opx}$. The Hf/Zr data fall on the 1:1 line, emphasising the coherent geochemical behaviour of this pair of "twins". In contrast, $D_{Nb}^{cpx/opx} > D_{Ta}^{cpx/opx}$, while also $D_{Th}^{cpx/opx} > D_{U}^{cpx/opx}$ (see Fig. 11b).

The partitioning of Ti, Zr and Nb between cpx and ol is plotted as a function of inverse temperature in Fig. 12 (Hf, Ta, Th and U are generally below detection limits in ol). Unlike for the REEs, the values of $D_{HFSE}^{cpx/ol}$ do not define a clear linear trend with $1/T_{(opx,\ 1.5GPa)}$. This is not due to analytical errors, as the amounts of Ti in olivine are orders of magnitude above detection limits and should be accurately determined. There is experimental evidence (Hermann et al., 2005) that the mode of Ti substitution in olivine changes as a function of temperature and H_2O fugacity; at high temperatures in an anhydrous environment, Ti substitutes

for Si on the tetrahedral site, whereas at low temperature in the presence of H_2O the substitution of Ti is into the octahedral site (i.e., similar to the titanoclino-humite structural unit). The parallel behaviour of Zr and Nb (Fig. 12) indicate that these trace elements may behave similarly.

5.4. Sr, Ba and Pb

These elements form large-radius divalent cations that are expected to substitute for Ca^{2+} in minerals. Their ionic radii in 8-fold coordination (from Shan-
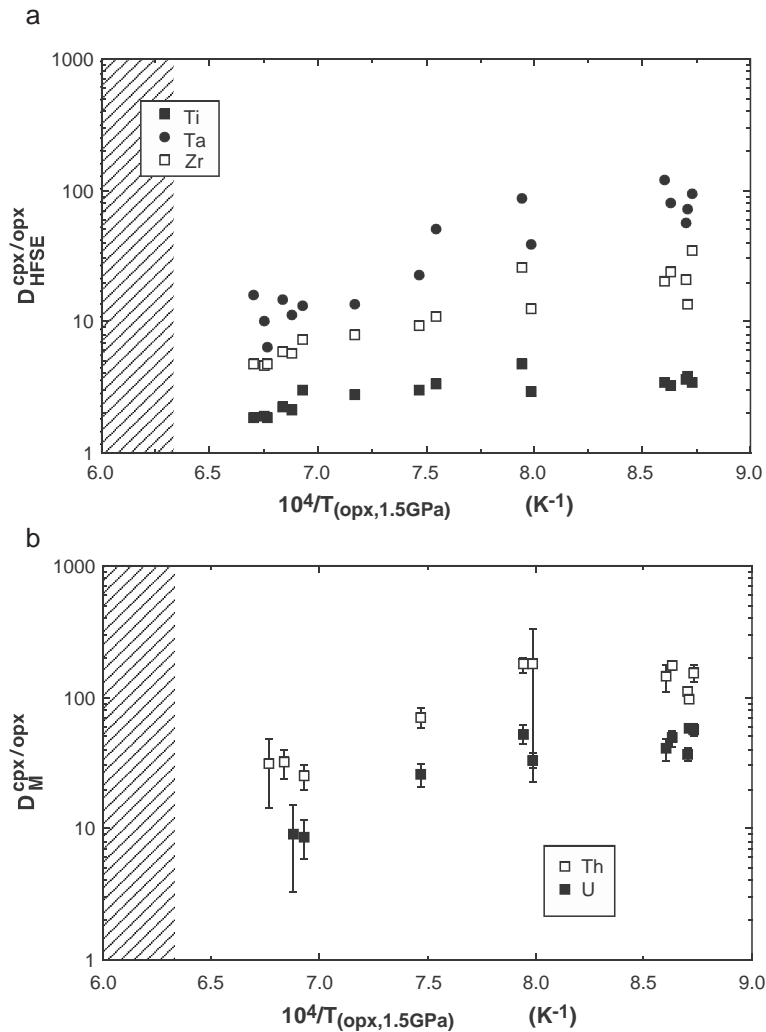
Fig. 11. Temperature dependence of the partitioning between cpx and opx of a) Ti, Zr and Ta; and b) U and Th. The data for Hf and Nb are not shown for clarity since they define trends very similar to that for Zr. The important point is that at magmatic temperatures (shaded region), a substantial part of the HFSE inventory will be held in opx. Note also that $D_{Th}^{cpx/opx} > D_{U}^{cpx/opx}$ at a given temperature.

non, 1976) increase in the order Ca (112 pm) < Sr (118 pm) < Pb (129 pm) < Ba (149 pm). The partitioning of Sr between cpx and opx shows a regular trend with temperature (Fig. 13); the array lies parallel to and in between those of the lightest REEs, La and Ce, although Sr is usually thought to have an incompatibility (i.e., bulk mineral/melt partition coefficient) that is in between Pr and Nd (Sun and McDonough, 1989). The greater preference of Sr for cpx over opx compared to Ca fits with simple crystal-chemical expectations that the larger cation would be preferentially

incorporated into the mineral with the larger crystallographic site, namely the M2 site in cpx. It is therefore surprising to find that Pb is much more evenly partitioned between cpx and opx than Ca or Sr, and extrapolation of the present data suggests that Pb may even prefer opx at magmatic temperatures (Fig. 13). However, considering the propensity of Pb to contaminate surfaces and the low levels of Pb in opx, this behaviour is in need of further confirmation. Nevertheless, if real, this behaviour may be due to the compressibility of the Pb^{2+} cation; the high atomic
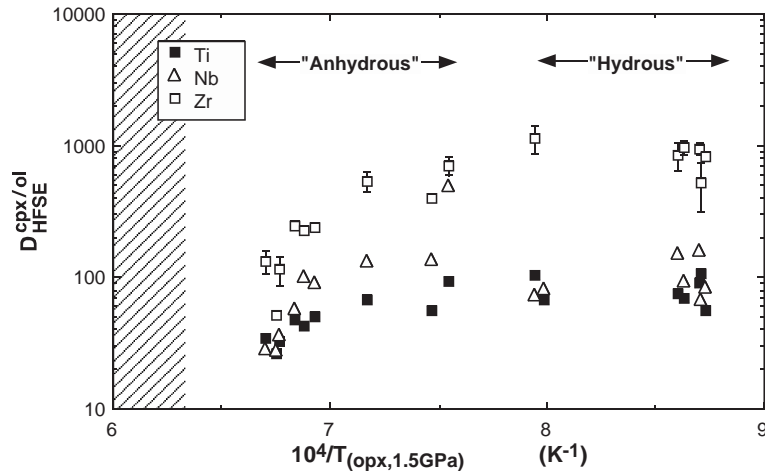
Fig. 12. Temperature dependence of the partitioning between cpx and ol of Ti, Zr and Nb. Unlike for the partitioning of these elements between cpx and opx, or for REE partitioning between cpx and ol, there is no well-defined trend with temperature. In the case of Ti, there is independent evidence to suggest that substitution into ol occurs by two different mechanisms depending on whether H_2O is present, thus the structural control on Ti partitioning (and by extension Zr and Nb) may be different in the hydrous versus the anhydrous xenoliths.

number of Pb means that the outer electrons are shielded from the nucleus by more shells of inner electrons than in Ca or Sr. This should lead to Pb anomalies on Onuma diagrams, as previously noted by Blundy and Wood (1994). In keeping with this explanation, the values of $D_{Ba}^{cpx/opx}$ are intermediate between $D_{Sr}^{cpx/opx}$ and $D_{Pb}^{cpx/opx}$ (Fig. 13), although

the data are rather scattered due to the low levels of Ba in opx.

5.5. Phosphorus

Phosphorus is another unusual element among the more incompatible trace elements, in that the
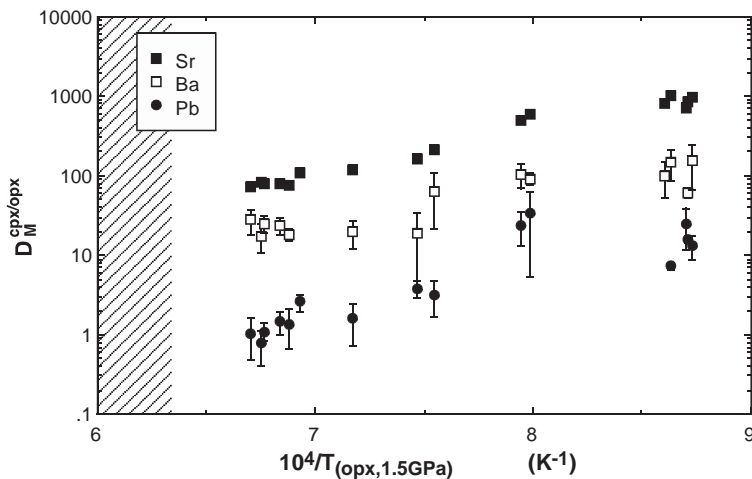
Fig. 13. Partitioning of divalent large-ion lithophile elements (Sr, Ba and Pb) between cpx and opx. The uncertainties (1 s.d.) on $D_{Sr}^{cpx/opx}$ are close to the size of the symbols and have not been plotted for clarity. The clear decrease in the order $D_{Sr}^{cpx/opx} > D_{Ba}^{cpx/opx} > D_{Pb}^{cpx/opx}$ is not expected from the simple argument from cation radii (which increase in the order $Sr^{2+} < Pb^{2+} < Ba^{2+}$) and crystal-chemical considerations that the largest cation, Ba^{2+}, would show the most preference for the enlarged M2 site in cpx. Instead, these data point to the compressibility of a cation being a significant factor in determining their partitioning behaviour.

phase with the highest P abundance is ol rather than cpx in anyhydrous spinel lherzolites; the sequence of P contents is generally amph > ol ≥ cpx > opx ≫ sp (Table 3; see also Brunet and Chazot, 2001), although incerature-dependent trends for the partition coefficients are not obvious (Fig. 14). The data for $P_P^{cpx/opx}$ and $D_P^{cpx/ol}$ appear to show a kink versus temperature between the anydrous and the amphibole-bearing samples (i.e., between Groups I+II and III+IV, Table 2) that might indicate that the substitution mechanism in cpx in the hydrous samples is different from that in the anhydrous samples. The partitioning between ol and opx is somewhat more regular (Fig. 14), with $D_P^{opx/ol}$ increasing with temperature to ~1 at the dry solidus. An approximate relationship is:

$$D_P^{opx/ol} = 0.84 - 2204/T$$

The value of χ_v^2 for the regression is 6.5 even after omitting one aberrant datum, DW1342 (Fig. 14); hence this cannot be considered a good fit. The implication is that the details of the partitioning of P may depend on coupled substitutions involving minor components (for example H_2O) not accounted for in Eq. (1), which are needed to provide the charge-balance for the substitution of P^{5+} for Si^{4+} in silicates.

5.6. Nickel and cobalt

Ni and Co substitute for the major-elements Mg and Fe^{2+} in all four phases of a spinel lherzolite, forming simple solid solutions with nearly ideal thermodynamic mixing properties (e.g., Seifert and O'Neill, 1987). The partitioning of both Ni and Co between olivine and orthopyroxene has been experimentally investigated by von Seckendorff and O'Neill (1994) in the systems $MgO–FeO–SiO_2 \pm NiO \pm CoO$ at 900–1600°C and 2.0 GPa. These experiments consisted of quasi-reversals (i.e., paired experiments starting with both high Ni or Co and low Ni or Co), and used a $BaO–B_2O_3$ flux (see von Seckendorff and O'Neill, 1993). Most runs were near $X_{Mg}^{ol}=0.9$ composition, but the effect of Mg/Fe^{2+} ratio was also investigated. The results can be summarized as:

$$\ln KD_{Ni/Mg}^{ol/opx} = 1419/T - 0.241$$

$$\ln KD_{Co/Mg}^{ol/opx} = (771 + 400X_{Fe}^{ol})/T - 0.094$$

These equations are based on 37 and 34 experiments, respectively. The Ni series included one
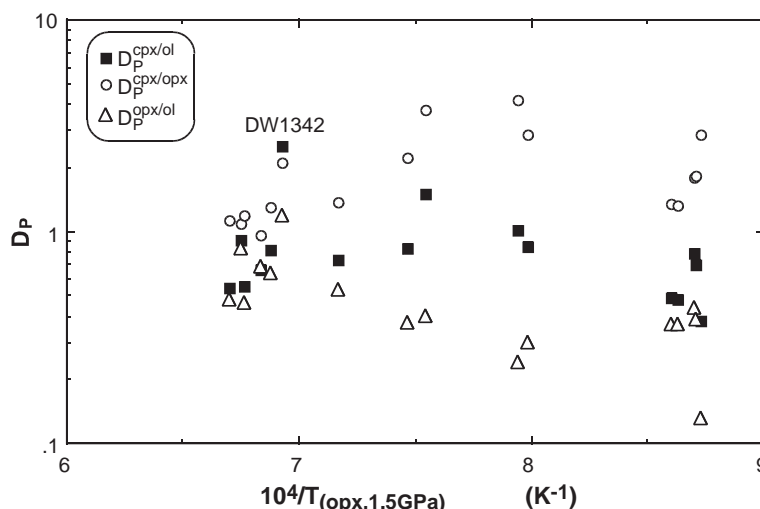
Fig. 14. Partitioning of P among cpx, opx and ol. This trace element is more evenly distributed among the silicate phases of lherzolite than most other incompatible trace elements, probably because it substitutes for Si, present as main constituent of all these phases. However in detail the distribution coefficients fit poorly to a simple correlation with temperature, suggesting the influence of other components that are needed to charge-balance the P/Si substitution.

multi-anvil run at 9.0 GPa confirming that the effect of pressure is negligible. That a term in X_{Fe}^{ol} is required to fit the Co data, but not the Ni data, is consistent with the observation that mixing of Mg and Ni in olivines is ideal but mixing of Mg and Co is similar to that of Mg and Fe in showing small positive deviations from ideality (Seifert and O'Neill, 1987).

The observed distribution coefficients from the xenoliths (Table 3) are compared to the experiments in Fig. 15a,b. For the Mg–Ni exchange reaction there is complete agreement, for the Mg–Co reaction the empirical data plot about 10% lower in $KD_{Co/Mg}^{ol/opx}$ than predicted from the experiments. The reason for this is unknown. A possibility is that Al_2O_3 ($\pm Cr_2O_3$) in opx, which was not included in
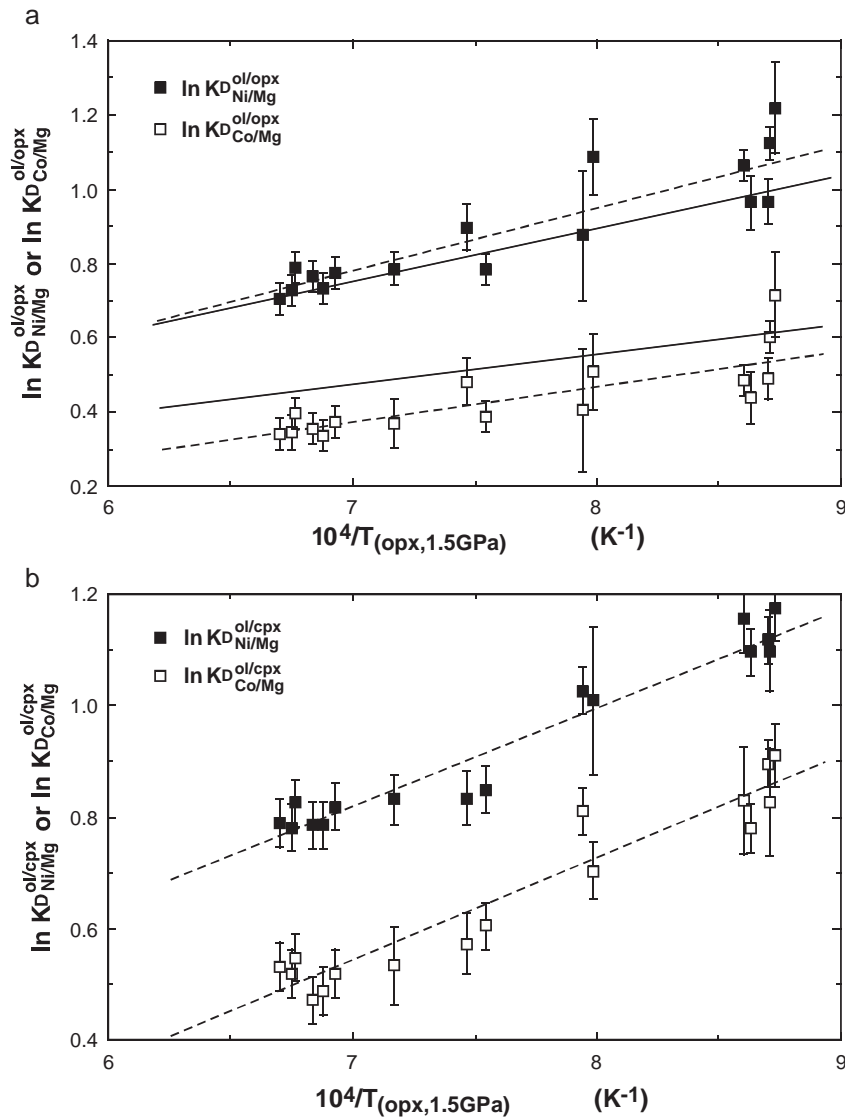
Fig. 15. a) Distribution of Ni and Mg and Co and Mg between olivine and orthopyroxene as a function of temperature. Solid lines summarize the experimental study of von Seckendorff and O'Neill (1994); dashed lines are empirical fits to the present data. b) Distribution of Ni and Mg and Co and Mg between olivine and clinopyroxene as a function of temperature. Dashed lines are empirical fits to the data.

the experimental study, may affect matters, but there is no obvious correlation between the magnitude of the discrepancy and Al in opx in the present xenolith data. Regression of the present data (Table 3) gives:

$$\ln KD_{Ni/Mg}^{ol/opx} = 1703/T_{(BKN\ opx)} - 0.419$$

$$\ln KD_{Co/Mg}^{ol/opx} = 940/T_{(BKN\ opx)} - 0.286$$

These empirical fits are also given in Fig. 15a,b for comparison.

For $KD_{Ni/Mg}^{ol/opx}$, both the experimental results of von Seckendorff and O'Neill (1994) and the present data are in excellent agreement with the pioneering empirical SIMS study of Hervig et al. (1980) on trace-element partitioning in mantle xenoliths. These latter authors obtained $\ln KD_{Ni/Mg}^{ol/opx} = 1630/T_{(Wells)} - 0.333$, based on the Wells (1977) two-pyroxene geothermometer.

The distribution coefficients for Mg–Ni and Mg–Co partitioning between ol and cpx are similarly sensitive to temperature, and can be described by the equations:

$$\ln KD_{Ni/Mg}^{ol/cpx} = 1773/T - 0.422$$

$$\ln KD_{Co/Mg}^{ol/cpx} = 1857/T - 0.758$$

The interesting feature of the partitioning of Mg and Ni between ol and sp is that the distribution coefficient varies strongly with the Cr content of the spinel, as well as temperature. The empirical fit gives:

$$\ln KD_{Ni/Mg}^{ol/sp} = (1722Cr\#^{sp})/T - 1.118$$

The sensitivity to $Cr\#^{sp}$ is not unexpected, because spinel is a reciprocal solid solution (Wood and Nicholls, 1978), with a large positive free energy for the reciprocal reaction:

$$NiAl_2O_4 + MgCr_2O_4 = NiCr_2O_4 + MgAl_2O_4 \qquad (7)$$
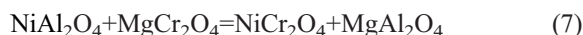
The positive free energy is caused by the relative instability of $NiCr_2O_4$, due to the very large octahedral site preference of Cr^{3+} forcing Ni^{2+}, itself with a well-known preference for octahedral coordination, onto the tetrahedral site of the spinel. The partitioning of Mg and Co between ol and sp also depends on $Cr\#^{sp}$, but in the opposite way—i.e., increasing $Cr\#^{sp}$ increases Co in spinel, which must be due to the relatively high stability of $CoCr_2O_4$ (similar to $FeCr_2O_4$). The partitioning is well described by the equation:

$$\ln KD_{Co/Mg}^{ol/sp} = (-1536 - 1179Cr\#^{sp})/T$$

5.7. Chromium, vanadium and gallium

These three elements occur mainly as the 3+ cations in systems pertinent to the Earth's mantle, although other oxidation states are possible in anomalously reducing or oxidizing environments for Cr and V, but not Ga (i.e., Cr^{2+} and V^{2+}, V^{4+} and perhaps V^{5+}); the occurrence of these other oxidation states can be expected to have important consequences for the geochemical behaviour of these elements, e.g., as shown by Seifert and Ringwood (1988) for the lunar geochemistry of Cr and V. Chromium needs to be treated as a major element in peridotitic systems, since the activity of Cr_2O_3 has a large effect on the solubility of Al_2O_3 in pyroxenes. Klemme and O'Neill (2000) studied the partitioning of Cr and Al between orthopyroxene and spinel in the system $MgO–Al_2O_3–SiO_2–Cr_2O_3$ experimentally, but found that the kinetics of the system were so sluggish that decent results could not be obtained below 1300 °C. The present data, therefore, are potentially valuable in that such well equilibrated, compositionally homogeneous xenoliths constitute natural experiments that can guide extrapolation of the laboratory experimental results to lower temperatures, and into more chemically complex systems.

Klemme and O'Neill (2000) found that the partitioning of Cr between orthopyroxene and spinel can be represented by the exchange reaction:

$$\underset{spinel}{MgAl_2O_4} + \underset{opx}{MgCr_2SiO_6} = \underset{spinel}{MgCr_2O_4} + \underset{opx}{MgAl_2SiO_6}$$

$$(8)$$
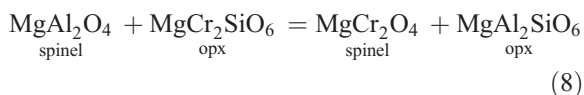
This defines $KD_{Al/Cr}^{opx/sp}$ as $([Al_2O_3]^{opx}/[Al_2O_3]^{sp})([Cr]^{sp}/([Cr]^{opx})$. The important point is that using $MgCrAlSiO_6$ as a pyroxene component does not fit the data well, despite its reasonableness as deduced

from crystallographic principles. From the data in Table 3 we obtain:

$$\ln KD_{Al/Cr}^{opx/sp} = (1215 + 3137 Cr\#^{sp})/T - 0.391$$
$$\left(\chi_v^2 = 0.74\right)$$

The small value of χ_v^2 shows that the data are well fitted by this simple model. Furthermore, the magnitude of the term in $Cr\#^{sp}$ is similar to that expected from a more rigorous thermodynamic treatment of reaction (8), as this term is equivalent to the Margulles interaction parameter for mixing in the join $MgAl_2O_4$–$MgCr_2O_4$ ($W_{Al-Cr}^{sp}/R = 2377$ K from Klemme and O'Neill, 2000). Further comparison of these results with the simple-system experiments is beyond the scope of this paper, as the addition of FeO to the system is expected to have a large effect by stabilizing Cr in spinel relative to pyroxene, as well as decreasing the total amount of Al_2O_3 plus Cr_2O_3 dissolved in pyroxene.

The partitioning of Cr and Al between opx and cpx is shown in the plot of ln $KD_{Al/Cr}^{cpx/opx}$ vs. $1/T$ in Fig. 16. There are now a large number of melting experiments of natural spinel lherzolite compositions that include studies with significant Cr in pyroxenes (Falloon et al., 1999, Pickering-Witter and Johnston, 2000; Schwab and Johnston, 2001) and also in the system CMAS-Cr_2O_3 (Liu and O'Neill, 2004); these show that $KD_{Al/Cr}^{cpx/opx}$ is ~1 at solidus temperatures in the

range 10–2.0 GPa, which is consistent with the trend displayed in Fig. 16. However, the present data show that Cr distributes preferentially into cpx with cooling below the solidus. Fitting all the data in the above-mentioned experimental studies (76 data) gives:

$$\ln KD_{Al/Cr}^{cpx/opx} = \left(-1141 - 2302 N_{Na}^{cpx} \right)/T + 0.905$$

The influence of N_{Na}^{cpx} implies a non-zero free energy for the reciprocal reaction $CaCr_2Si_2O_6 + 2\ NaAlSi_2O_6 = CaAl_2Si_2O_6 + 2\ NaCrSi_2O_6$ in cpx, although this parameter is not constrained well from the presently available data, which are all at low or zero N_{Na}^{cpx}.

The amount of Cr in olivine ($[Cr]^{ol}$, here given in ppm) is very sensitive to temperature (Fig. 17), as previously emphasised by Stosch (1981) and Hervig and Smith (1982); the curiosity here is the relative insensitivity of $[Cr]_{ol}$ to $Cr\#^{sp}$, which compositional parameter reflects the activity of Cr_2O_3 in each xenolith. A working hypothesis is that the thermodynamics of the substitution of Cr in olivine, unlike that in pyroxenes, is indeed controlled directly by charge-coupling with Al, according to a reaction of the type:

$$1/2\ \underset{spinel}{MgCr_2O_4} + 1/2\ \underset{spinel}{MgAl_2O_4} = \underset{olivine}{MgCrAlO_4} \quad (9)$$

In this case $[Cr]_{ol}$ would be proportional to the product $(Cr^{sp})(1 - Cr\#^{sp})$ rather than just simply proportional to $Cr\#^{sp}$, and a semi-empirical model
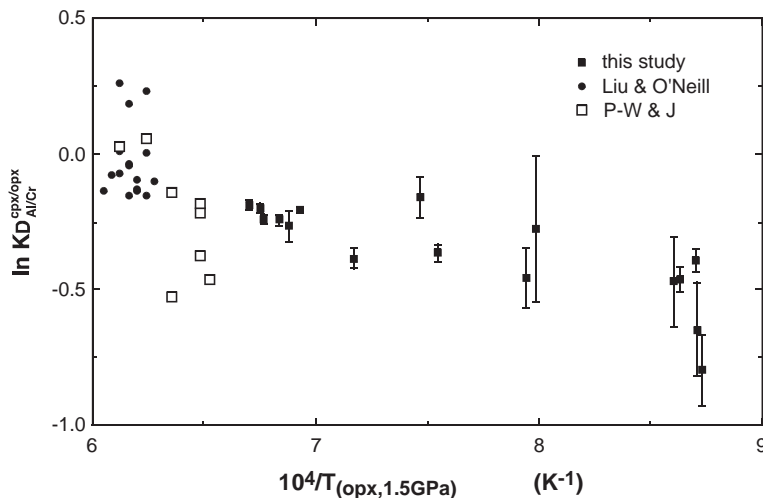
Fig. 16. Two-element distribution coefficient $KD_{Al/Cr}^{cpx/opx}$ compared to data from supra-solidus experiments in the system CMAS-Cr_2O_3 (Liu and O'Neill, 2004), and Cr-rich natural compositions (Pickering-Witter and Johnston, 2000). At magmatic temperatures $KD_{Al/Cr}^{cpx/opx}$ is close to 1, apparently independent of Cr/Al ratios (Liu and O'Neill, 2004), but with falling temperature cpx gains a higher Cr/Al ratio compared to opx.
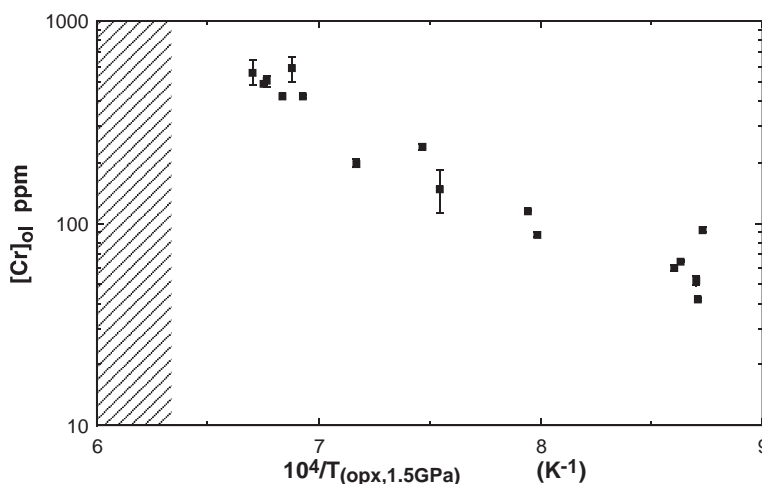
Fig. 17. The Cr content of olivine, $[Cr]_{ol}$, as a function of temperature. Although both $Cr\#^{sp}$ and potentially fO_2 influence $[Cr]_{ol}$, these effects appear subsidiary to temperature. Hence the Cr content of an olivine makes a useful guide to temperature.

incorporating this functional form was found to give a better fit to the data. Assuming the form of reaction Eq. (9), we obtain:

$$\ln[Cr]_{ol} = \ln Cr\#^{sp}(1 - Cr\#^{sp}) - 10070/T + 14.47$$

although χ_v^2 is 5.3, with the uncertainty in $[Cr]_{ol}$ taken as 5% or as observed, whichever is larger. Unfortunately we did not determine the Al contents of olivines, so are not able to test this hypothesis further.

Although there can be extensive substitution of Cr^{2+} in olivine at very high temperatures or very low oxygen fugacity (Li et al., 1995), circumstantial evidence argues against significant Cr^{2+} in the olivine of these xenoliths. Firstly, there is no perceptible dependence of $[Cr]^{ol}$ on $\Delta \log fO_2$, although this may be because the range of covered by the xenoliths is not large. More convincingly, there is a remarkable coherence in the partitioning of Cr and V between all four phases, as illustrated, for example, by the parallel behaviour of $D_{Cr}^{opx/ol}$ and $D_V^{opx/ol}$ (Fig. 18); this suggests that Cr and V share the same oxidation state in every phase.

It is known from the previous work of Hervig and Smith (1982) that the trend for $D_{Cr}^{opx/ol}$ vs. $1/T$ may look reasonably coherent in a suite of spinel lherzolites (Fig. 18a), but is different in garnet lherzolites, presumably due to the role of Al_2O_3 in providing the thermodynamic "stoichiometric control" on Cr solubi-

lities, as discussed above. The stoichiometric control for V is likely to be similar, suggesting that the partitioning of V can be treated accurately using two-element distribution coefficients with Cr. Regressions of our Cr and V data are entirely consistent with this, the results being:

$$\ln KD_{Cr/V}^{cpx/opx} = 864/T - 0.394 \qquad (\chi_v^2 = 1.1)$$

$$\ln KD_{Cr/V}^{cpx/ol} = 532/T - 0.329 \qquad (\chi_v^2 = 1.3)$$

$$\ln KD_{Cr/V}^{cpx/sp} = (3571 - 1163Cr\#^{sp})/T - 0.554$$
$$(\chi_v^2 = 1.8)$$

where the uncertainties in $KD_{Cr/V}^{\alpha/\beta}$ were calculated from the data in Table 2.

The behaviour of Ga is found to be very similar to that of Cr and V, with its concentration decreasing in the order sp $\gg$ cpx~opx $\gg$ ol. Unfortunately we chose to measure the ^{69}Ga isotope, which is affected slightly by an interference from ^{29}Si+^{40}Ar. A better choice would have been ^{71}Ga. Based on subsequent work on other xenoliths, the interference inflates the pyroxene abundances by ~0.2 ppm, which is a barely significant proportion of the amounts observed and has been ignored. However, the interference dominates the levels in ol (which is probably ~0.1 ppm); Ga abundances in ol are therefore not
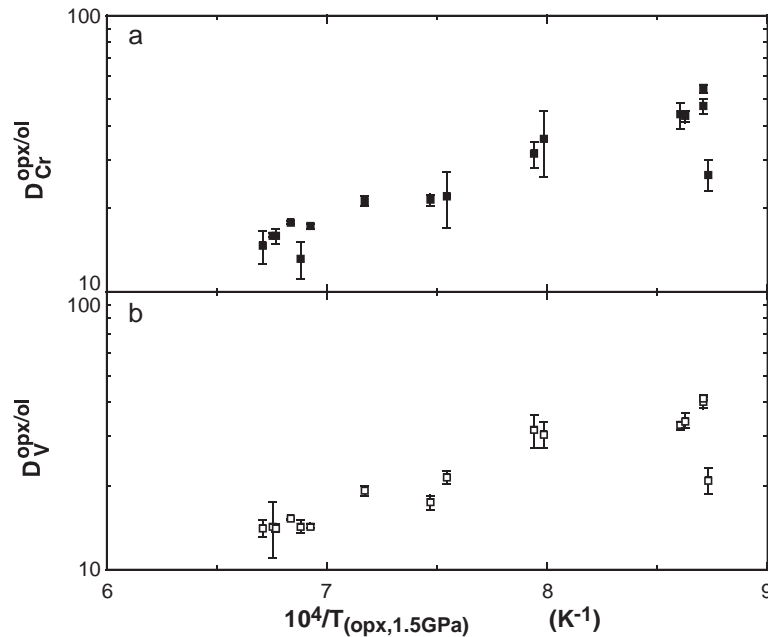
Fig. 18. Partitioning of a) Cr and b) V between opx and ol. Note the very good coherence between $D_{Cr}^{opx/ol}$ and $D_V^{opx/ol}$, suggesting that Cr and V share the same oxidation state (i.e., 3+) in both phases.

reported. Two-element distribution coefficients for Ga and Cr are:

$$\ln KD_{Cr/Ga}^{cpx/opx} = -1783/T + 0.790 \qquad (\chi_v^2 = 0.76)$$

$$\ln KD_{Cr/Ga}^{cpx/sp} = (-345 + 2635 Cr\#^{sp})/T - 0.137$$
$$(\chi_v^2 = 1.9)$$

Although the partitioning relations of V and Ga among the solid phases in spinel lherzolite are similar to those of Cr, the partitioning of V and Ga between these phases and silicate melt is quite different from that of Cr, with V and Ga being moderately incompatible whereas Cr is compatible. This suggests that consideration of Cr–V–Ga systematics may have the potential to be a useful tool in understanding basalt petrogenesis.

5.8. Amphibole

Amphibole is preserved in four of our xenoliths, two each in groups III and IV, which groups have equilibrated 100 K apart (Table 2). The amphibole is a chrome pargasite, in which Na_2O (+K_2O) is an essential structural component, with Na+K more-or-less

filling the A site. In cpx, by contrast, Na_2O behaves thermodynamically much like a trace-element component, being a relatively minor substitutant into the M2 site. Consequently the partitioning of Na between amphibole and cpx provides a good example of a partitioning relationship that is controlled by crystal chemistry rather than intensive thermodynamic variables such as temperature or pressure. The fact that N_{Na}^{cpx} changes by over a factor of two in the amphibole-bearing samples indicates that it is some component other than Na_2O that controls the amounts of amphibole, plausibly H_2O (see reaction Eq. (3) above).

That amphibole is in chemical equilibrium with the other peridotite minerals is attested to well by the smooth amph/cpx REE partitioning patterns, shown in Fig. 19. Three samples have flat patterns of $D_{REE}^{amph/cpx}$ vs. ionic radius (R_{REE}^{VIII}), the fourth (MM110) defines a very smooth linear trend in which $D_{REE}^{amph/cpx}$ decreases with decreasing R_{REE}^{VIII}. There is nothing obvious in the chemistry of the amphibole in MM110 to explain why it should behave differently. Apart from the heavy REEs in MM110, there is a remarkably good correlation of $D_{REE}^{amph/cpx}$ with N_{Na}^{cpx}, which is nearly quantitatively that expected from the
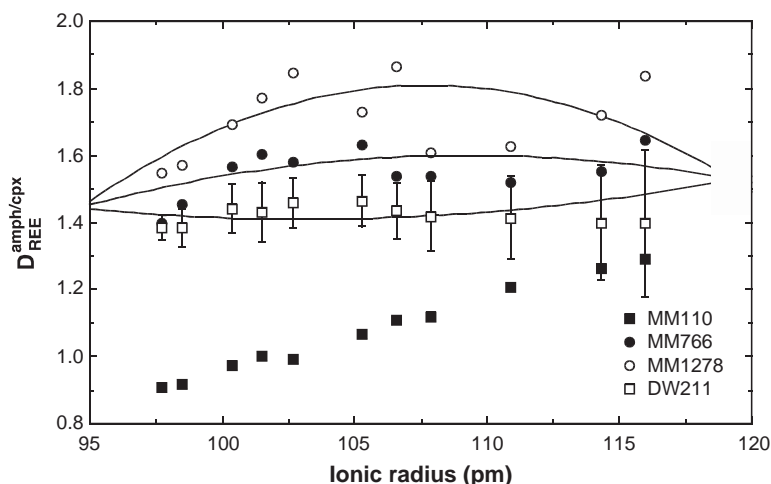
Fig. 19. Partitioning of REE between amphibole (amph) and cpx. The curves are the calculated fits from Eq. (9) in the text for MM1278, MM766 and DW211, respectively. The increase in values of $D_{REE}^{amph/cpx}$ correlates with decreasing N_{Na}^{cpx} in these four xenoliths.

influence of N_{Na}^{cpx} on cpx/opx and cpx/ol partitioning relations as given in Tables 4 and 5, except that the quadratic dependence of $D_{REE}^{cpx/opx}$ on N_{Na}^{cpx} is not evident (this should cause curved, not flat patterns). This might be rationalised by assuming that the curvature caused by the effect of Na in cpx is counterbalanced by a structural control in amphibole. In fact, the three samples with flat $D_{REE}^{amph/cpx}$ vs. IR can be fitted within analytical uncertainty to the expression:

$$\ln D_{REE}^{amph/cpx} = a_0 + b_0 R_{REE}^{VIII} + c_0 \left(R_{REE}^{VIII}\right)^2 \\ - \left(a_2 + b_2 R_{REE}^{VIII} + c_2 \left(R_{REE}^{VIII}\right)^2\right) N_{Na}^{cpx} \tag{10}$$

(cf. Eq. (5)), with the values of a_2, b_2 and c_2 constrained to the values from the global fit of the $D_{REE}^{cpx/opx}$ vs. IR data. These fits are shown in Fig. 19. The light REE in MM110 agree well with this fit, it is the decrease of heavy REE in the amphibole of this sample that is anomalous. Obviously, though, invoking the terms b_0 and c_0 to counterbalance the b_1 and c_2 terms is special pleading given the few data and further work is required.

The most distinctive features of amphibole trace-element chemistry are the enormous enrichments relative to cpx of the "large-ion lithophile elements" (LILEs) K, Rb and Ba. Among the HFSEs, Nb and Ta are also greatly enriched but Zr and Hf are not, and neither are Th and U. The values of $D_{Ba}^{amph/cpx}$ are

~10^3 (Rb is below detection limits in cpx, while K was not determined in this study, hence quantification of these partition coefficients is not possible), while values of $D_{Nb}^{amph/cpx}$ are ~10^2. The latter are considerably higher than values of $D_{Ta}^{amph/cpx}$, by about a factor of 4. All these peculiarities are well known, and almost exactly similar partitioning patterns have been observed previously in other mantle xenoliths containing coexisting amphibole and cpx (e.g., Lee et al., 1996; Glaser et al., 1999, their Fig. 6), and in comparisons of experimental determinations of amphibole/melt and cpx/melt partition coefficients (Brenan et al., 1995; Green, 1995). They mean that the role of amphibole in any mantle melting process should be obvious from anomalously low Ba/Th or Nb/Zr ratios. In particular, Ba would appear to become a compatible element if pargasitic amphibole is in the source.

6. Conclusions

Equations summarizing the intercrystalline partition coefficients for incompatible trace elements as a function of temperature are listed for $D_M^{cpx/opx}$ in Table 4, and for $D_M^{cpx/ol}$ in Table 5. These equations allow the amounts of these incompatible trace elements present in the minerals at magmatic temperatures to be calculated, if the modal amounts of cpx, opx and ol
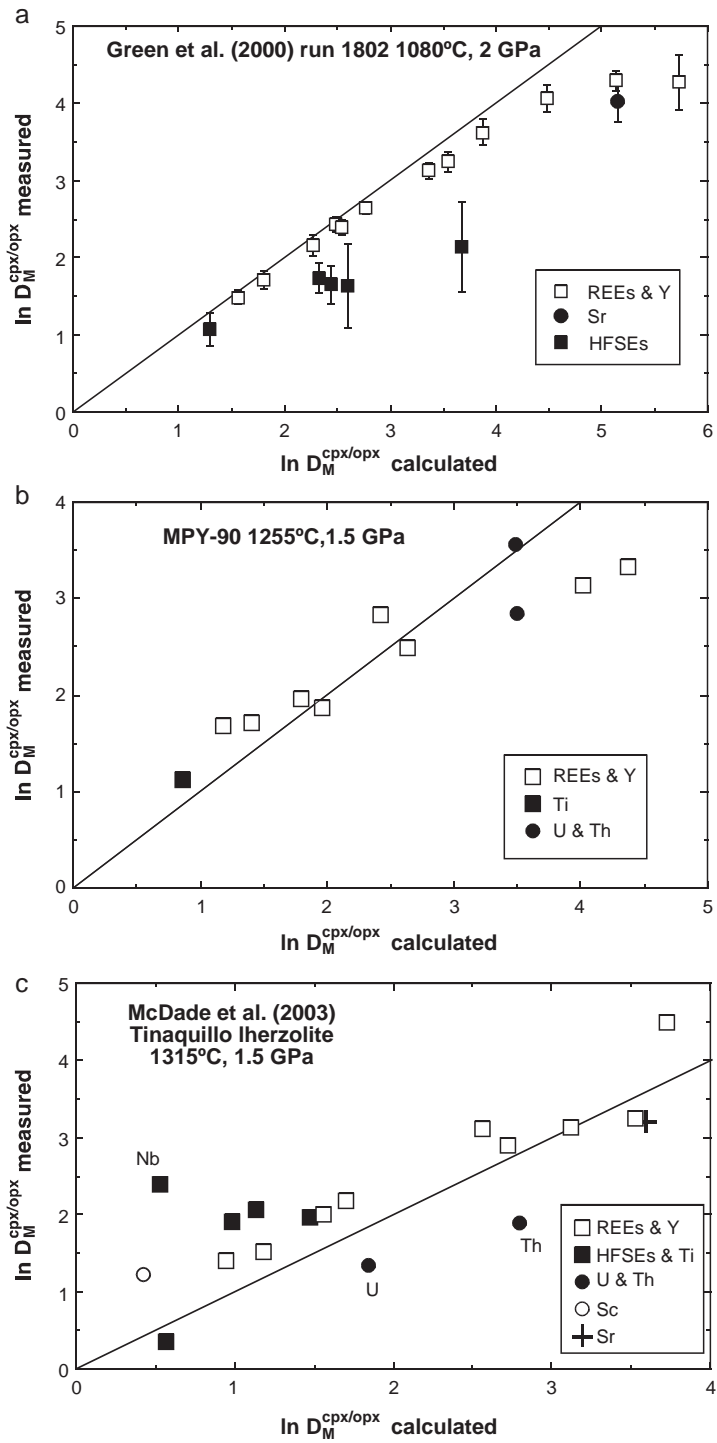
at this temperature are reconstructed from the major-element phase relations.

The equations in Table 4 may be evaluated for internal consistency with experimental work in which cpx/melt and opx/melt partition coefficients were measured in the same run, since $D_M^{cpx/opx} = D_M^{cpx/melt}/D_M^{opx/melt}$ at the temperature of the experiment. For example, in Fig. 20 a,b and c, we compare some experimental values of $D_M^{cpx/opx}$ for large suites of trace elements obtained in this way with our own results. Agreement is generally good, although there are some inconsistencies, the cause of which should become clearer as the experimental database on trace-element partitioning in multiply saturated phase assemblages increases.

A most important conclusion from this study is that opx can be a significant carrier of many incompatible trace elements at magmatic temperatures. In the case of the HFSEs (Ti and Zr), the role of opx as the host phase been pointed out previously by Rampone et al. (1991) and McDonough et al. (1992), from analyses of subsolidus re-equilibrated opx/cpx pairs as found in actual peridotites; but here we emphasise that opx will also host a substantial fraction of the whole-rock budget of other incompatible trace elements, when values of $D_M^{cpx/opx}$ are extrapolated back to magmatic temperatures.

In fact, it is a common assumption in the literature on the geochemistry of peridotites that cpx carries most of the whole-rock's incompatible trace elements. This may indeed be the case after subsolidus re-equilibration (with the exception of HFSEs, noted above), which permits using cpx analyses, obtained with SIMS or LA-ICP-MS, as a proxy for whole-rock values. But it is not then valid to use these measured subsolidus cpx concentrations with values for cpx/melt partition coefficients ($D_M^{cpx/melt}$) to calculate the melt trace-element abundances that were in equilibrium with the peridotite. The data presented here show that the temperature-dependence of cpx/opx and even cpx/ol partition coefficients results in significant fractions of incompatible trace elements being held in opx (± ol) at magmatic temperatures, which will repartition during subsolidus cooling into cpx. For example, the partition data plotted in Fig. 7 suggests that steeply sloping REE patterns in cpx, thought to be characteristic of "ultra-depleted" melts, could instead be generated by subsolidus re-equilibration of residual peridotite, in which the cpx is produced from the CaO that was held in opx and ol at the temperature of the melting regime.

The interpretation of cpx trace-element patterns (indeed, any kind of mineral trace-element pattern) in terms of equilibrium with a melt (or fluid) therefore requires not only the reconstruction of mineral compositions as a function of temperature, but also an estimate of the temperature at which the rock would have been in equilibrium with the melt or fluid. This requires that the major-element and volatile content of the melt or fluid and its stability relations be known. Disembodied trace-element data, divorced from their major-element contexts and considered in isolation from phase-equilibrium constraints, are likely to lead to erroneous conclusions.

Acknowledgments

Fig. 20. Comparison between experimentally measured values of $D_M^{cpx/opx}$ from the literature (calculated from $D_M^{cpx/opx} = D_M^{cpx/melt}/D_M^{opx/melt}$) and those calculated from the present study using the equations in Table 4. a) A hydrous melt at 1080 °C, 2 GPa from Green et al. (2000), their run 1802. Error bars from the experimental data are one standard deviation. Agreement is good for the REE except the lightest (La, Ce and Nd), but poorer for the HFSEs and Sr. b) MORB pyrolite (MPY) at 1255 °C, 1.5 GPa, data from Blundy et al. (1998) and unpublished (Jon Blundy, personal communication 2003), with Th and U from Wood et al. (1999); agreement is again good except for the lightest REE and U, with low concentrations in opx. c) Tinaquillo lherzolite at 1315 °C, 1.5 GPa, from McDade et al. (2003), their Table 4. Here agreement is less good, for unknown reasons.

References

Barth, M.G., Rudnick, R.L., Horn, I., McDonough, W.F., Spicuzza, M.J., Valley, J.W., Haggerty, S.E., 2001. Geochemistry of xenolithic eclogites from West Africa: Part I. A link between low MgO eclogites and Archean crust formation. Geochim. Cosmochim. Acta 65, 1499–1527.

Bedini, R.M., Bodinier, J.L., 1999. Distribution of incompatible trace elements between the constituents of spinel peridotite xenoliths: ICP-MS data from the East. Geochim. Cosmochim. Acta 63, 3383–3900.

Bertrand, P., Mercier, J.C.C., 1985. The mutual solubility of coexisting orthopyroxene and clinopyroxene—toward an absolute geothermometer for the natural system. Earth Planet. Sci. Lett. 76, 109–122.

Blundy, J.D., Wood, B.J., 1994. Prediction of crystal-melt partition coefficients from elastic moduli. Nature 372, 452–454.

Blundy, J.D., Robinson, J.A.C., Wood, B.J., 1998. Heavy REE are compatible in clinopyroxene on the spinel lherzolite solidus. Earth Planet. Sci. Lett. 160, 493–504.

Brenan, J.M., Shaw, H.F., Ryerson, F.J., Phinney, D.L., 1995. Experimental determination of trace-element partitioning between pargasite and a synthetic hydrous andesitic melt. Earth Planet. Sci. Lett. 135, 1–11.

Brey, G.P., Köhler, T., 1990. Geothermobarometry in 4-phase lherzolites: 2. New thermobarometers, and practical assessment of existing thermobarometers. J. Petrol. 31, 1353–1378.

Brunet, F., Chazot, G., 2001. Partitioning of phosphorus between olivine, clinopyroxene and silicate glass in a spinel lherzolite xenolith from Yemen. Chem. Geol. 176, 51–72.

Eggins, S.M., Rudnick, R.L., McDonough, W.F., 1998. The composition of peridotites and their minerals: a laser-ablation ICP-MS study. Earth Planet. Sci. Lett. 154, 53–71.

Falloon, T.J., Green, D.H., Danyushevsky, L.V., Faul, U.H., 1999. Peridotite melting at 1.0 and 1.5 GPa: an experimental evaluation of techniques using diamond aggregates and mineral mixes for determination of near-solidus melts. J. Petrol. 40, 1343–1375.

Gao, S., Liu, X., Yuan, H., Hattendorf, B., Günther, D., Chen, L., et al., 2002. Determination of forty two major and trace elements in USGS and NIST SRM glasses by Laser Ablation-Inductively Coupled Plasma-Mass Spectrometry. Geostand. Newsl. 26, 181–196.

Glaser, S.M., Foley, S.F., Günther, D., 1999. Trace element compositions of minerals in garnet and spinel peridotite xenoliths from the Vitim volcanic field, Transbaikalia, eastern Siberia. Lithos 48, 263–285.

Glassley, W.E., Piper, D.Z., 1978. Cobalt and scandium partitioning versus iron content for crystalline phases in ultramafic nodules. Earth Planet. Sci. Lett. 39, 173–178.

Green, T.H., 1995. Significance of NB/TA as an indicator of geochemical processes in the crust-mantle system. Chem. Geol. 120, 347–359.

Green, T.H., Blundy, J.D., Adam, J., Yaxley, G.M., 2000. SIMS determination of trace element partition coefficients between garnet, clinopyroxene and hydrous basaltic liquids at 2–7.5 GPa and 1080–1200 °C. Lithos 53, 165–187.

Halicz, L., Günther, D., 2004. Quantitative analysis of silicates using LA-ICP-MS with liquid calibration. J. Anal. At. Spectrom. 19, 1539–1545.

Hermann, J., O'Neill, H.St.C., Berry, A.J., 2005. Titanium solubility in olivine in the system TiO_2–MgO–SiO_2: no evidence for an ultra-deep origin of Ti-bearing olivine. Contrib. Mineral. Petrol. 148, 746–760.

Hervig, R.L., Smith, J.V., 1982. Temperature-dependent distribution of Cr between olivine and pyroxenes in lherzolite xenoliths. Contrib. Mineral. Petrol. 81, 184–189.

Hervig, R.L., Smith, J.V., Steele, I.M., 1980. Fertile and barren Al-Cr spinel harzburgites from the upper mantle-ion and electron-probe analyses of trace-elements in olivine and ortho-pyroxene-relation to lherzolites. Earth Planet. Sci. Lett. 50, 41–58.

Hirschmann, M.M., 2000. Mantle solidus: experimental constraints and the effects of peridotite composition. Geochem., Geophys., Geosystems 1 (paper no. 2000GC000070).

Köhler, T., Brey, G.P., 1990. Calcium exchange between olivine and clinopyroxene calibrated as a geothermobarometer for natural peridotites from 2 to 60 kb with applications. Geochim. Cosmochim. Acta 54, 2375–2388.

Klemme, S., O'Neill, H.St.C., 2000. The effect of Cr on the solubility of Al in orthopyroxene: experiments and thermodynamic modelling. Contrib. Mineral. Petrol. 140, 84–98.

Lee, D.-C., Halliday, A.N., Davies, G.R., Essene, E.J., Fitton, J.G., Temdjim, R., 1996. Melt enrichment of shallow depleted mantle: a detailed petrological, trace element and isotopic study of mantle-derived xenoliths and megacrysts from the Cameroon Line. J. Petrol. 37, 415–441.

Li, J.-P., O'Neill, H.St.C., Seifert, F., 1995. Subsolidus phase relations in the system MgO–SiO_2–Cr–O in equilibrium with metallic Cr, and their significance for the petrochemistry of chromium. J. Petrol. 36, 107–132.

Liu, X., O'Neill, H.St.C., 2004. The effect of Cr_2O_3 on the partial melting of spinel lherzolite in the system CaO–MgO–Al_2O_3–SiO_2–Cr_2O_3 at 1.1 GPa. J. Petrol. 45, 2261–2286.

McCammon, C.A., Griffin, W.L., Shee, S.R., O'Neill, H.St.C., 2001. Oxidation during metasomatism in ultramafic xenoliths from the Wesselton kimberlite, South Africa: implications forthe survival of diamond. Contrib. Mineral. Petrol. 141, 287–296.

McDade, P., Blundy, J.D., Wood, B.J., 2003. Trace element partitioning on the Tinaquillo lherzolite solidus at 1.5 GPa. Phys. Earth Planet. Inter. 139, 129–147.

McDonough, W.F., Stosch, H.-G., Ware, N., 1992. Distribution of titanium and the rare earth elements between peridotitic minerals. Contrib. Mineral. Petrol. 110, 321–328.

Mechie, J., Prodehl, C., Fuchs, K., 1983. The long-range seismic refraction experiment in the Rhenish Massif. In: Fuchs, K., von Gehlen, K., Mälzer, H., Murawski, H., Semmel, A. (Eds.), Plateau Uplift. Springer, Berlin, pp. 260–275.

Norman, M.D., Griffin, W.L., Pearson, N.J., Garcia, M.O., O'Reilly, S.Y., 1998. Quantitative analysis of trace element abundances in glasses and minerals: a comparison of laser ablation inductively coupled plasma mass spectrometry, solu-

tion inductively coupled plasma mass spectrometry, proton microprobe and electron microprobe data. J. Anal. At. Spectrom. 13, 477–482.

O'Neill, H.St.C., Eggins, S.M., 2002. The effect of melt composition on trace element partitioning: an experimental investigation of the activity coefficients of FeO, NiO, CoO, MoO_2 and MoO_3 in silicate melts. Chem. Geol. 186, 151–158.

O'Neill, H.St.C., Palme, H., 1998. Composition of the silicate Earth: implications for accretion and core formation. The Earth's Mantle: Structure, Composition and Evolution. Cambridge University Press, New York, pp. 3–126.

O'Neill, H.St.C., Wall, V.J., 1987. The olivine–orthopyroxene–spinel oxygen geobarometer, the nickel precipitation curve, and the oxygen fugacity of the earth's upper mantle. J. Petrol. 28, 1169–1191.

O'Reilly, S.Y., Griffin, W.L., Ryan, C.G., 1991. Residence of trace-elements in metasomatised spinel lherzolite xenoliths—a proton-microprobe study. Contrib. Mineral. Petrol. 109 (1), 98–113.

Pickering-Witter, J., Johnston, A.D., 2000. The effects of variable bulk composition on the melting systematics of fertile peridotitic assemblages. Contrib. Mineral. Petrol. 140, 190–211.

Press, S., Witt, G., Seck, H.A., Ionov, D., Kovalenko, V.I., 1986. Spinel peridotite xenoliths from the Tariat Depression, Mongolia: I. Major element chemistry and mineralogy of a primitive mantle xenolith suite. Geochim. Cosmochim. Acta 50, 2587–2599.

Raikes, S., Bonjer, K.P., 1983. Large-scale mantle heterogeneity beneath the Rhenish Massif and its vicinity from teleseismic P-residuals measurements. In: Fuchs, K., von Gehlen, K., Mälzer, H., Murawski, H., Semmel, A. (Eds.), Plateau Uplift. Springer, Berlin, pp. 315–331.

Rampone, E., Bottazzi, P., Ottolini, L., 1991. Complementary Ti and Zr anomalies in orthopyroxene and clinopyroxene from mantle peridotites. Nature 354, 518–520.

Salters, V.J.M., Longhi, J.E., Bizimis, M., 2002. Near mantle solidus trace element partitioning at pressures up to 3.4 GPa. Geochem. Geophys. Geosystems 3 (Art no 1038).

Schwab, B.E., Johnston, A.D., 2001. Melting systematics of modally variable, compositionally intermediate peridotites and the effects of mineral fertility. J. Petrol. 42 (10), 1789–1811.

Seifert, S., O'Neill, H.St.C., 1987. Experimental determination of activity–composition relations in Ni_2SiO_4–Mg_2SiO_4 and Co_2SiO_4–Mg_2SiO_4 olivine solid solutions at 1200 K and 0.1 MPa and 1573 K and 0.5GPa. Geochim. Cosmochim. Acta 51, 97–104.

Seifert, S., Ringwood, A.E., 1988. The lunar geochemistry of chromium and vanadium. Earth Moon, Planets 40, 45–70.

Seitz, H.M., Altherr, R., Ludwig, T., 1999. Partitioning of transition elements between orthopyroxene and clinopyroxene in peridotitic and websteritic xenoliths: new empirical geothermometers. Geochim. Cosmochim. Acta 63, 3967–3982.

Shannon, R.D., 1976. Revised effective ionic radii and systematic studies of interatomic distances in halides and chalcogenides. Acta Crystallogr. A32, 751–767.

Stosch, H.G., 1981. Sc, Cr, Co and Ni partitioning between minerals from spinel peridotite xenoliths. Contrib. Mineral. Petrol. 78, 166–174.

Stosch, H.G., 1982. Rare-earth element partitioning between minerals from anhydrous spinel peridotite xenoliths. Geochim. Cosmochim. Acta 46, 793–811.

Stosch, H.G., Lugmair, G.W., Kovalenko, V.I., 1986. Spinel peridotite xenoliths from the Tariat Depression, Mongolia: 2. Geochemistry and Nd and Sr isotopic composition and their implications for the evolution of the subcontinental lithosphere. Geochim. Cosmochim. Acta 50, 1614–2601.

Sun, S.-S., McDonough, W.F., 1989. Chemical and isotopic systematics of oceanic basalts: implications for mantle composition and processes. In: Saunders, A.D., Norry, M.J. (Eds.), Magmatism in the Ocean Basins, Geological Society Special Publication, vol. 42, pp. 313–345.

van Orman, J.A., Grove, T.L., Shimizu, N., 2001. Rare earth element diffusion in diopside: influence of temperature, pressure, and ionic radius, and an elastic model for diffusion in silicates. Contrib. Mineral. Petrol. 141, 687–703.

von Seckendorff, V., O'Neill, H.St.C., 1993. Distribution of Ni between olivine, orthopyroxene and metal phase between 900 degrees C and 1600 degrees C at 2 GPa. Terra Abstr. 5 (Suppl. 1), 408–409.

von Seckendorff, V., O'Neill, H.St.C., 1994. Distribution of Ni and Co between olivine and orthopyroxene between 900 °C at 2 GPa. Terra Nova 6 (Abstract Suppl. 1), 50.

Wells, P.R.A., 1977. Pyroxene thermometry in simple and complex systems. Contrib. Mineral. Petrol. 62, 129–139.

Witt, G., Seck, H.A., 1987. Temperature history of sheared mantle xenoliths from the West Eifel, West Germany: evidence for mantle diapirism beneath the Rhenish Massif. J. Petrol. 28, 475–493.

Witt-Eickschen, G., Harte, B., 1994. Distribution of trace-elements between amphibole and clinopyroxene from mantle peridotites of the Eifel (Western Germany)—an ion-microprobe study. Chem. Geol. 117, 235–250.

Witt-Eickschen, G., Kramm, U., 1997. Mantle upwelling and metasomatism beneath central Europe: geochemical and isotopic constraints from mantle xenoliths from the Rhon (Germany). J. Petrol. 38, 493–497.

Witt-Eickschen, G., Kramm, U., 1998. Evidence for the multiple stage evolution of the subcontinental lithospheric mantle beneath the Eifel (Germany) from pyroxenite and composite pyroxenite/peridotite xenoliths. Contrib. Mineral. Petrol. 131, 258–272.

Witt-Eickschen, G., Seck, H.A., Reys, C.H., 1993. Multiple enrichment processes and their relationships in the subcrustal lithosphere beneath the Eifel (Germany). J. Petrol. 34, 1–22.

Witt-Eickschen, G., Seck, H.A., Mezger, K., Eggins, S.M., Altherr, R., 2003. Lithospheric mantle evolution beneath the Eifel (Germany): constraints from Sr–Nd–Pb isotopes and trace element abundances in spinel peridotite and pyroxenite xenoliths. J. Petrol. 44, 1077–1095.

Wood, B.J., Nicholls, J., 1978. The thermodynamic properties of reciprocal solid solutions. Contrib. Mineral. Petrol. 66, 389–400.

Wood, B.J., Blundy, J.D., Robinson, J.A.C., 1999. The role of clinopyroxene in generating U-series disequilibrium during mantle melting. Geochim. Cosmochim. Acta 63, 1613–1620.